Damage due to Liquefaction and Associated Lateral Flow during the 2024 Noto Peninsula Earthquake, Japan

By

Hemanta Hazarika, Shotaro Kubota, Anurag Sahare, Shiro Ohta, Tsuyoshi Tanaka, Tomohiro Ishizawa, Masanori Murai, Takashi Fujishiro, Yuji Michi, Yutao Hu, Taichi Hyodo, Tatsunori Matsumoto, Takaji Kokusho

A report prepared by Kyushu University, Kawasaki Geological Engineering Co., Ltd, Tokyo City University, National Research Institute for Earth Science and Disaster Resilience, Shimizu Corporation, Geo Disaster Prevention Institute, Yoshimitsugumi Inc., Kyushu University, Toyama Prefectural University, Kanazawa University, Chuo University in cooperation with Geotechnical Extreme Event Reconnaissance Association

GEER Association Report 084

doi.org/10.18118/G61T1J

February 24, 2025

Damage due to Liquefaction and Associated Lateral Flow during the 2024 Noto Peninsula Earthquake, Japan

Table of Contents

Acknowledgements

The authors would like to express their sincere gratitude for the financial supports provided by the President's Special Research Fund of Kyushu University and Short Term Joint Research Fund of the Institute of Mathematics for Industry (IMI), Kyushu University. We also wish to acknowledge the generous cooperation of the Department of Education and the Department of Construction, Uchinada Town, during the course of our investigation. Special appreciation is extended to Mr. Shinpei Taniguchi, Mr. Tomonari Ohyama and Ms. Rui Takahashi of Yoshimitsugumi Inc., Komatsu; Dr. Chengjiong Qin of IMAGEi Consultant, Tokyo; and Mr. Yoshikazu Ochi of Kawasaki Geological Engineering Co., Ltd., Kyushu Branch for their significant assistance during the field tests and data analysis. Lastly, the authors would like to express their deep gratitude to Mr. Kaoru Mizuno of Uchinada Town, for his generous support in facilitating the field survey and providing essential data and information throughout our investigations.

Executive Summary

On January 1, 2024, at 16:10 JST, a powerful earthquake of moment magnitude 7.5 struck the Noto Peninsula in southeastern Japan, with its epicenter located in Suzu City, Ishikawa Prefecture. The earthquake caused widespread destruction across Ishikawa, Fukui, Toyama, and Niigata prefectures. Significant damage was inflicted on low-rise buildings, roads, utilities, port facilities, and other critical infrastructure. The transportation network on the Noto Peninsula was severely disrupted by slope and embankment failures, hindering recovery efforts. The earthquake also induced extensive soil liquefaction, resulting in considerable geotechnical and structural damage. Liquefaction was not confined to the coastal areas near the epicenter but was observed in more distant regions of Ishikawa Prefecture and in neighboring prefectures as well. Uchinada Town, located on gently sloping reclaimed land in Ishikawa Prefecture, was particularly impacted, with substantial lateral spreading causing severe damage to low-rise buildings, roads, and public utilities. To gain a deeper understanding of the underlying mechanisms of the widespread liquefaction and the associated damage in Uchinada, a joint investigation team consisting of researchers and engineers from academia, government, and industry was assembled one month after the earthquake. The team conducted a series of surveys in Uchinada and surrounding areas from February to August 2024. The survey includes UAV Photogrammetry, 3D Laser Scanning, Portable Dynamic Cone Penetration Test, Screw Driver Sounding Test, Piezo Drive Cone Test, Surface Wave Exploration, and Standard Penetration Test. This report describes the detailed findings of the investigation and presents a factorial analysis of the extensive lateral displacement responsible for the damage infrastructures in the area. To mitigate liquefaction-induced damage in the region during future earthquakes, the report also delineates some of the key challenges.

1. Introduction

On January 1, 2024, at 16:10 JST, a powerful earthquake struck the Noto Peninsula in southeastern Japan, with its epicenter located in Suzu City, Ishikawa Prefecture. The earthquake caused widespread damage across Ishikawa, Fukui, Toyama, and Niigata prefectures. According to the Japan Meteorological Agency (JMA), the event had a JMA magnitude (Mj) of 7.6 (moment magnitude Mw 7.5), a focal depth of approximately 16 km, and a reverse fault mechanism characterized by a northwest-southeast compression axis.

The earthquake was preceded by a foreshock of magnitude 5.7 and followed by 8,582 aftershocks, the largest registering a magnitude of 6.1. The main shock caused extensive damage to low-rise buildings, roads, utilities, port facilities, and critical infrastructure. Slope and embankment failures severely disrupted transportation networks on the Noto Peninsula, complicating recovery efforts. The earthquake also triggered a tsunami, with wave heights reaching up to 6.58 meters along the Sea of Japan coastline.

This earthquake was Japan's deadliest since the 2011 Great East Japan Earthquake, claiming 412 lives and injuring 1,300 people (Fire and Disaster Management Agency, 2024). Approximately 90% of the fatalities were attributed to falling debris from heavily damaged buildings. The disaster affected 168,822 structures, with the Japanese government estimating economic losses at $17.6 billion USD.

In Wajima City, the earthquake sparked a devastating fire that destroyed 200 buildings, including the Asaichi morning market and a nearby shopping district. In Suzu City, the epicenter, approximately 90% of buildings were damaged, with wooden structures suffering the most severe impact.

The earthquake triggered extensive soil liquefaction and numerous landslides, leading to significant geotechnical damage across Ishikawa Prefecture and the neighboring prefectures. Figure 1.1 illustrates the areas impacted by soil liquefaction and landslides during the event.

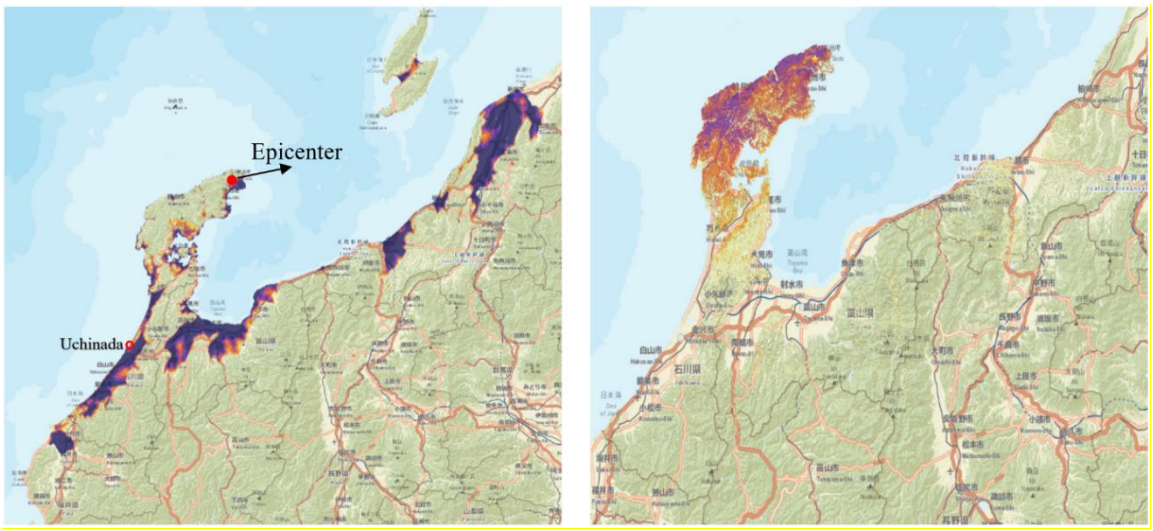

(a) Liquefaction induced damage (b) Landslides induced damage

Figure 1.1. Areas in Noto-Peninsula of Japan affected by earthquake-induced soil liquefaction and landslides (source: USGS)

The occurrence of soil liquefaction was not confined to coastal areas near the earthquake's epicenter; it was also observed in distant regions such as Uchinada Town, approximately 100 km south of the epicenter, as well as Toyama Prefecture, 60 km to the southeast, Fukui Prefecture, 200 km to the southwest, and Niigata Prefecture, 160 km to the northeast. As shown in Figure 1(a), the effects of liquefaction were particularly severe near Uchinada Town in Ishikawa Prefecture, where significant liquefaction-induced lateral spreading occurred due to the presence of gently sloping sand dunes. This widespread distribution of liquefaction highlights the extensive impact of the earthquake. While local ground conditions contributed to the observed effects, the primary driver of such widespread liquefaction was the intense ground motion generated by the rupture of a fault approximately 130 km in length.

To investigate the mechanisms behind the widespread liquefaction and the resulting damage to low-rise buildings, infrastructure, and public utilities, a collaborative team of researchers and engineers from academia, government, and industry was established under the leadership of the first author. The team conducted multiple surveys in Uchinada Town between February 2024 and August 2024, with preliminary findings reported in Hazarika et al (2024) including several reports (Fujishiro et al., 2024; Hazarika et al., 2024; Hu et al., 2024; Kubota et al., 2024a, 2024b, 2024c; Michi et al., 2024; Murai et al., 2024; Sahare et al., 2024). This report presents a detailed investigation of the phenomenon, including a factorial analysis of the substantial lateral displacement of structures, through two focused case studies.

2. Seismological history of Noto Peninsula

2.1 Topography and Geology Overview

The Noto Peninsula and its surrounding coastal areas are situated within an active fault zone, which has been the source of significant seismic events, including the 1993 Noto Peninsula Offshore Earthquake, the 2007 Noto Peninsula Earthquake, and the 2024 Noto Peninsula Earthquake (hereinafter referred to as the "present earthquake"). These events underscore the region's vulnerability and highlight the need for disaster prevention measures (Ozaki et al., 2019). Furthermore, the Noto Peninsula holds a key position in the geological history of the Sea of Japan, which formed over a span of approximately 30 million years, marking the separation of the Eurasian continent from the Japanese archipelago. The formation of the Sea of Japan began in the middle Oligocene (around 30 million years ago) and continued into the middle Early Miocene (around 18 million years ago). A rising mantle plume caused the continental crust along the eastern margin of Eurasia to stretch, resulting in the formation of normal faults and subsequent ruptures in the crust. This activity allowed large volumes of magma to erupt from the subsurface through these fractures, triggering an increase in volcanic activity. From the end of the Early Miocene (around 18 million years ago) to the end of the Late Miocene (around 6 million years ago), the crust continued to stretch, leading to the expansion of the Japan Sea and the eventual complete separation of the Japanese islands from Eurasia. Between 18 and 15 million years ago, the Japan Sea rapidly expanded and deepened, and this deep-sea state persisted thereafter. Shallow to deep-sea sediments from this period are widely distributed across the Noto Peninsula, as illustrated in Figure 2.1.

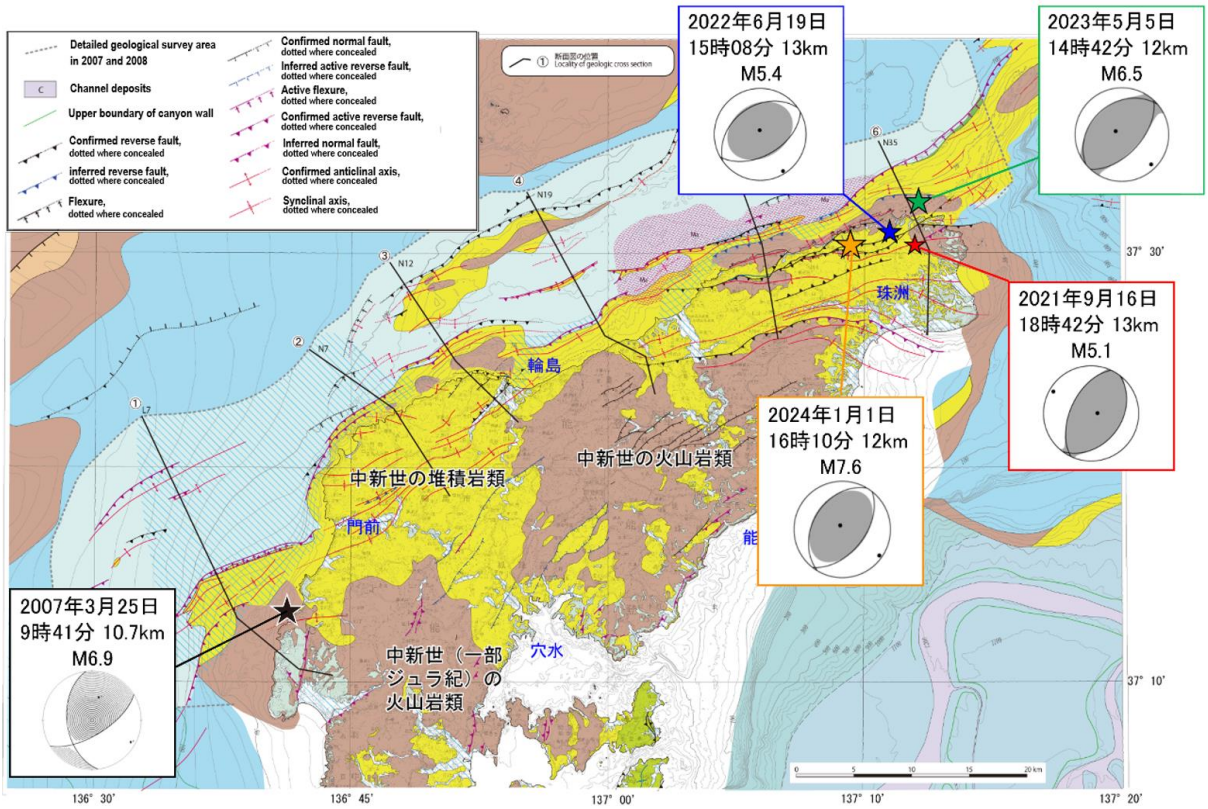

Figure 2.1. Seamless geological map of the sea and the land of the Noto Peninsula and the distribution of the epicenters (Ozaki et al., 2019)

The topography of the Noto Peninsula has been extensively described by Ota and Hirakawa (1979) and Machida et al. (2006), including the formation of marine terraces and tectonic movements. The northwestern region of the peninsula is characterized by hilly or mountainous terrain, whereas the eastern and southern regions predominantly feature marine terraces, with approximately 20 distinct terraces identified. Some of these marine terraces reach elevations of up to 400 meters, suggesting that their formation dates back to the Early Pleistocene. Ongoing active crustal deformation is evident, as demonstrated by the recent earthquake, which caused a coastal uplift of 3.8 to 3.9 meters.

2.2 Active Faults

Figure 2.2 illustrates the distribution of active faults in the Noto Peninsula and its coastal region. Active faults are primarily concentrated in the northern part of the peninsula and the adjacent sea areas along the northern coastline. The development of these faults is especially prominent in coastal areas, where certain faults have likely been active for approximately 20,000 years, exhibiting displacements of more than 20 meters. This translates to an average displacement rate exceeding 1 meter per thousand years. All active submarine faults in the region are reverse faults that dip to the southeast.

In April 2024, three months following the earthquake, the GSJ conducted a seismic reflection survey. Preliminary results indicated widespread new fault displacements, with up to 3–4 meters of uplift observed on the southeastern side of the fault. The extent of displacement is still under investigation.

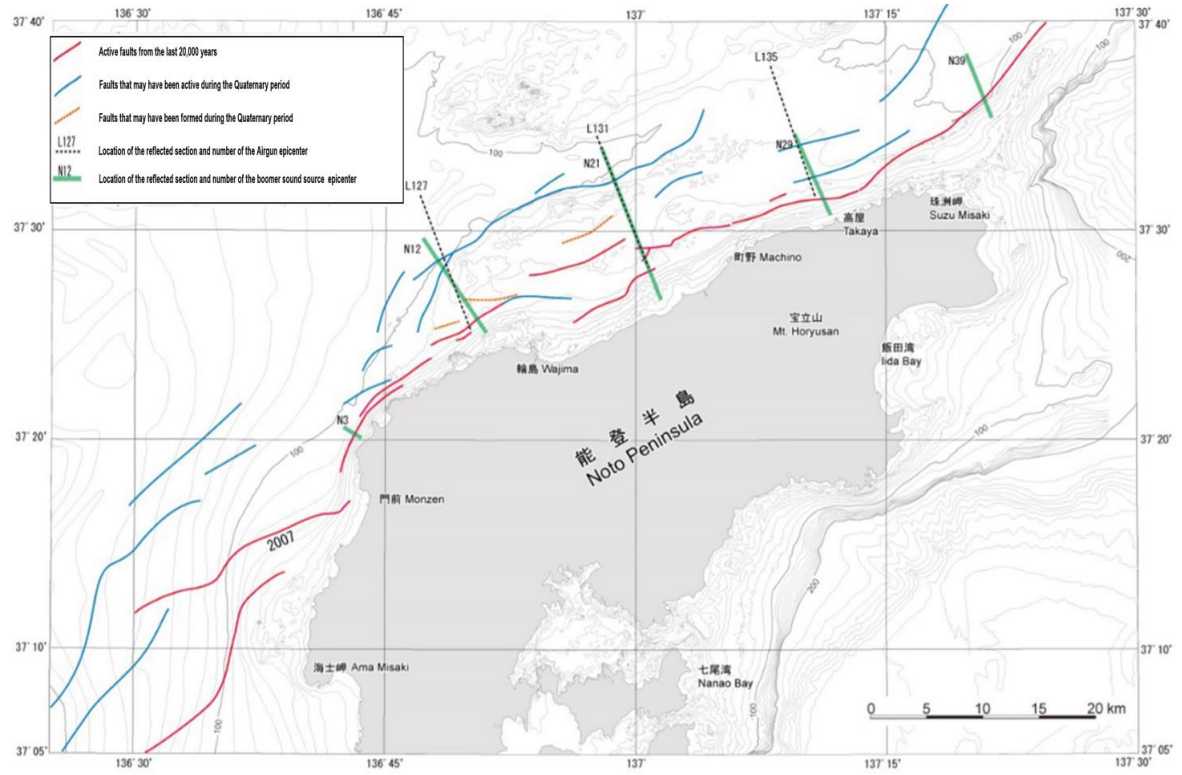

Figure 2.2. Structural map of the coastal waters of the northern Noto Peninsula (Inoue & Okamura, 2010)

3. Ground Motion Characteristics of the earthquake

3.1 Earthquake Mechanism

The 2024 Noto Peninsula Earthquake, with its epicenter located in the northern part of the Noto Peninsula, was marked by its considerable magnitude and widespread spatial impact. Figure 3.1 illustrates the epicentral distribution of the mainshock and subsequent aftershocks, based on data analyzed by the National Research Institute for Earth Science and Disaster Resilience (NIED, 2024). The seismic activity extended approximately 150 km, spanning from the southwest to the northeast of the peninsula. Notably, intense seismic activity was concentrated in the area between Wajima City and Suzu City.

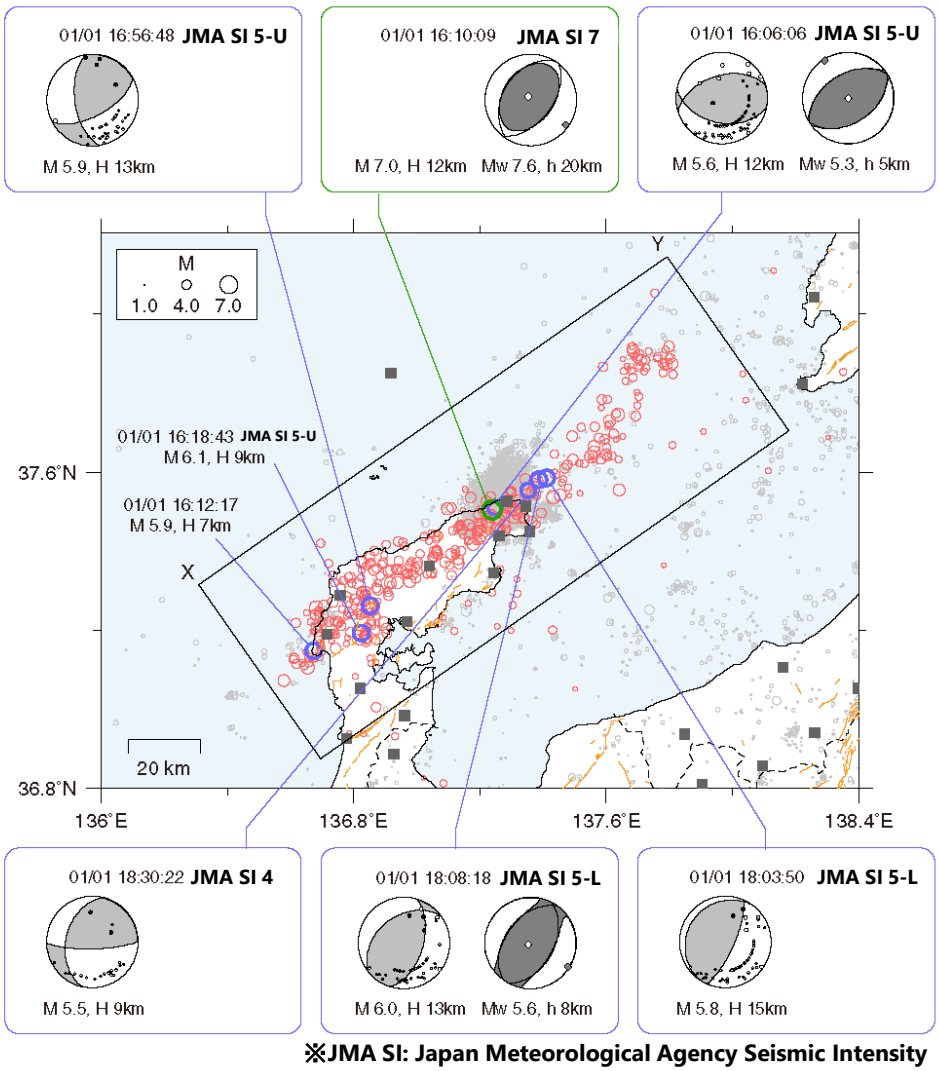

Figure 3.1. Epicentral distribution of the mainshocks and aftershocks (NIED, 2024)

Figure 3.2 presents the results of source inversion analysis using strong-motion waveform records, as conducted by NIED (2024). Figure 3.2(a) illustrates the surface projection of the final slip distribution on the fault plane, while Figure 3.2(b) shows the slip distribution directly on the fault plane. The fault model comprises three rectangular fault segments. The rupture

process analysis identified significant activity in the shallow regions of the northeast (fault plane #1) and southwest (fault planes #2 and #3) relative to the rupture initiation point. The rupture process exhibited a complex temporal evolution. During the first 15 seconds after the onset, no substantial rupture was detected. Subsequently, rupture initiated in the shallow region of fault plane #2, followed by the activation of shallow regions in fault planes #1 and #3 approximately 30 seconds after the onset. The maximum slip observed was estimated at 5.3 meters.

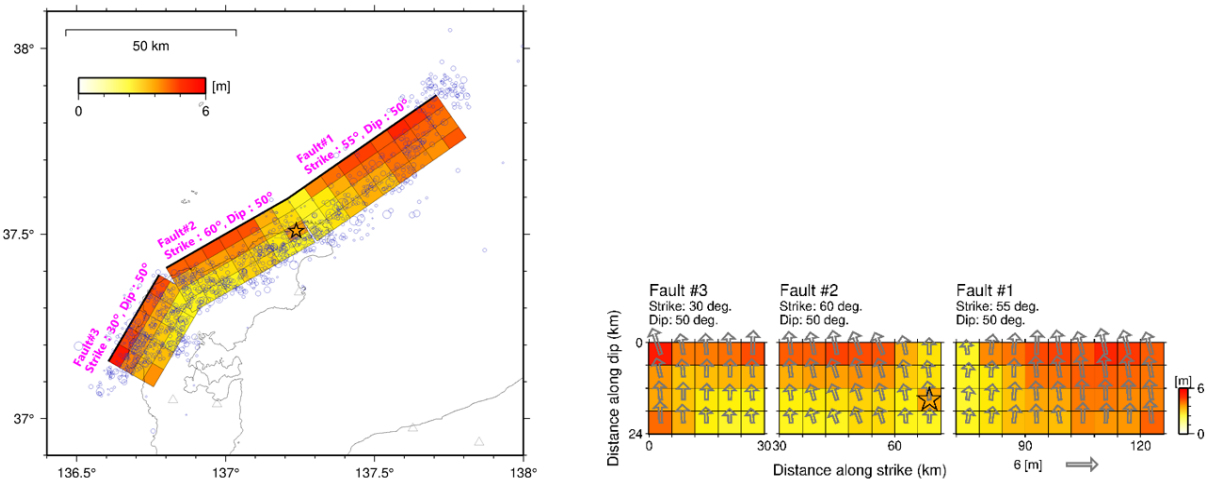

(a) Surface projection of slip distribution (b) Slip distribution on the fault plane

Figure 3.2. Source inversion analysis (based on waveforms recorded by NIED)

3.2 Ground Motion Characteristics

A notable characteristic of this seismic event was the extended duration of ground motion, which caused widespread damage across a vast area. According to the Japan Meteorological Agency (JMA, 2024), a seismic intensity of 7 on the JMA scale was recorded in Wajima City and Shika Town, near the epicenter. The tremors were felt over an extensive region, with a seismic intensity of 1 reported as far as Hokkaido in northern Japan and the Kyushu region in the south. The Noto Peninsula, located near the epicenter, experienced intensities ranging from 7 to 6-Lower, while Nagaoka City in Niigata Prefecture, approximately 140 km southeast of the epicenter, recorded an intensity of 6-Lower.

Figure 3.3 illustrates the distribution of Peak Ground Acceleration (PGA) measured at various strong-motion stations within the NIED strong-motion seismograph network (NIED, 2024) during the mainshock. The figure also highlights the epicenter, the estimated fault model, locations of slope failures, and areas affected by liquefaction. The slope failure data were derived from the deposition distribution dataset provided by the Geospatial Information Authority of Japan (GSI, 2024), while liquefaction occurrence sites were identified based on the report by Senna (2024).

Remarkably, seven sites near the source fault in Suzu City, Wajima City, Anamizu Town, and Shika Town in Ishikawa Prefecture recorded PGA values exceeding 1000 Gal (1 Gal = 1 cm/s²). Among these, the K-NET Togi station (ISK006) reported an exceptionally high PGA of 2828 Gal, comparable to the 2933 Gal recorded during the 2011 Great East Japan Earthquake (Mw

9.0). Although PGA alone does not fully characterize the intensity of shaking, the elevated PGA values corresponded to extensive structural damage near the fault. Numerous building collapses were documented, and frequent slope failures were observed, particularly in proximity to fault planes #2 and #3, located southwest of the epicenter.

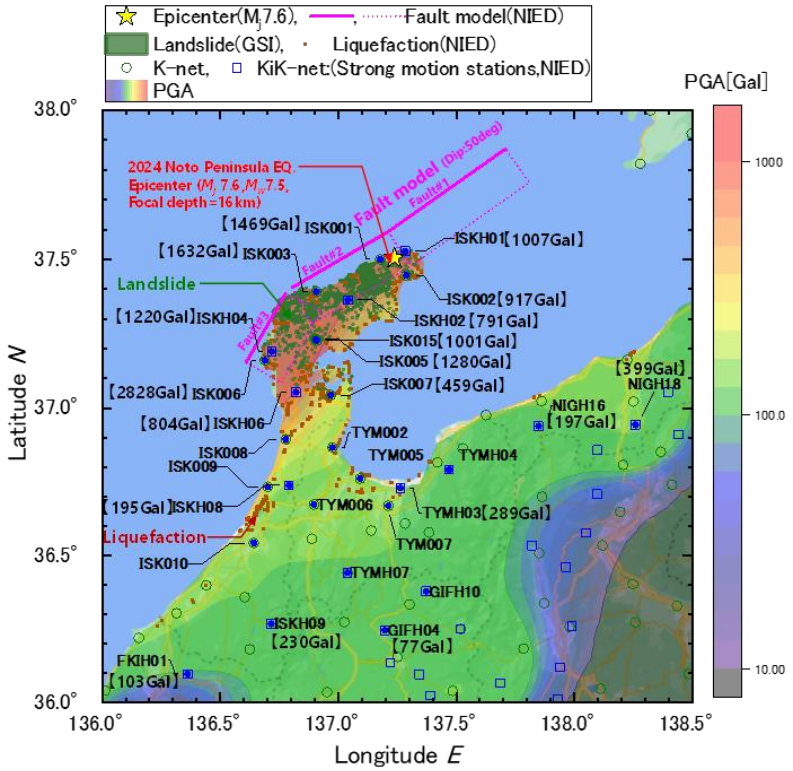

Figure 3.3. Distribution of Peak Ground Acceleration (PGA) with areas experiencing soil liquefaction and slope failures during the 2024 Noto-Peninsula mainshock

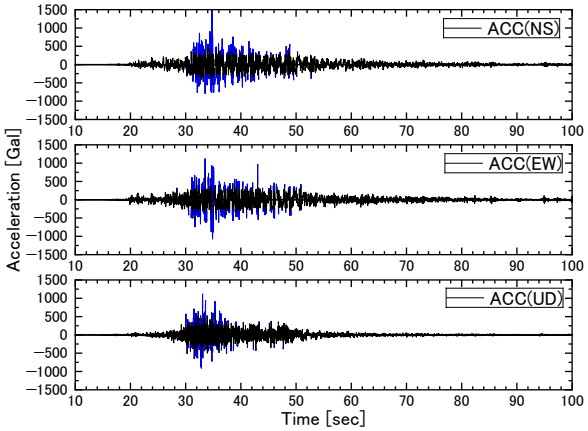

Figure 3.4. Acceleration-time history data recorded at K-NET Wajima (ISK003)

Figure 3.4 depicts the strong-motion record from the K-NET Wajima station (ISK003), which recorded a PGA of 1632 Gal. This site experienced significant building damage, liquefaction, and landslides. The figure highlights that high accelerations, exceeding ±250 Gal, persisted for over 15 seconds—a duration considerably longer than typical for inland earthquakes of

comparable magnitude. Source inversion analysis indicates a rupture process characterized by stepwise and widespread propagation, a distinctive mechanism likely responsible for the prolonged strong shaking observed over a broad area.

Table 3.1 provides a summary of the characteristics of 11 strong-motion stations situated near the fault, with epicentral distances ranging from 2 to 60 km and surface S-wave velocities varying between 90 and 440 m/s. In the near-fault region, no clear correlation was identified between epicentral distance and key ground motion parameters such as PGA or Peak Ground Velocity (PGV)..

Table 3.1. Characteristics of strong-motion stations near the fault

Strong motion station (K-NET, KiK-net)		Epicenter distance R0 (km)	S-wave velocity V_s (m/s)	Peak ground acceleration PGA (cm/s^2 = Gal)	Peak ground velocity PGV (cm/s)
ISK006	Togi	59	260	2828	84
ISK003	Wajima	28	230	1632	104
ISK001	Ohtani	2	200	1469	110
ISK005	Amamizu	40	120	1280	149
ISKH04	Togi	55	440	1220	85
ISKH01	Suzu	8	240	1007	148
ISK015	Ohmachi	40	120	1001	105
ISK002	Syoin	10	110	917	137
ISKH06	Shika	60	240	804	45
ISKH02	Yanagida	21	420	791	64
ISK007	Nanao	55	90	459	33

Figure 3.5 presents the results of velocity response spectrum analysis (5% damping ratio) derived from horizontal acceleration records (NS and EW components) at the surface for the stations near the fault, as listed in Table 3.1. Figure 3.5(a) illustrates the locations of the analyzed K-NET and KiK-net stations. Figures 3.5(b) and 3.5(c) provide the velocity response spectra for stations near fault planes #2 and #3, respectively.

Figure 3.5(b) displays the spectra for stations near fault planes #1 and #2, revealing notable variations in response patterns. Stations K-NET Wajima (ISK003), K-NET Ohtani (ISK001), and KiK-net Suzu (ISKH01), located above these fault planes, exhibited peak periods ranging from 1.0 to 2.0 seconds, with response values exceeding 250 cm/s. In contrast, K-NET Syoin (ISK002) displayed a peak period of approximately 3 seconds, suggesting the influence of local site effects. KiK-net Yanagida (ISKH02) demonstrated unique spectral characteristics, with differing peak periods of 1.8 seconds (NS component) and 0.77 seconds (EW component).

Both components recorded high response values exceeding 400 cm/s, indicative of intense ground motion.

Figure 3.5(c) focuses on stations near fault plane #3, where distinct ground motion characteristics were observed. Stations K-NET Anamizu (ISK005), KiK-net Shika (ISKH06), and K-NET Nanao (ISK007) exhibited peak periods in the range of 1.0 to 2.0 seconds. Among these, ISK005 was particularly notable, with high-velocity response values exceeding 500 cm/s in the 2-second range. By comparison, K-NET Ohmachi (ISK015), located approximately 700 m from ISK005, showed significantly lower response values of 180–270 cm/s in the 1-second peak period range. This discrepancy in ground motion characteristics between the two closely located stations can be attributed to differences in their subsurface geology. ISK005 is underlain by soft, highly organic soil within the top 10 m, whereas ISK015 features bedrock at a depth of 2 m. These contrasting geological conditions are inferred to be the primary factors contributing to the observed differences in the periodic characteristics of ground motion at these locations.

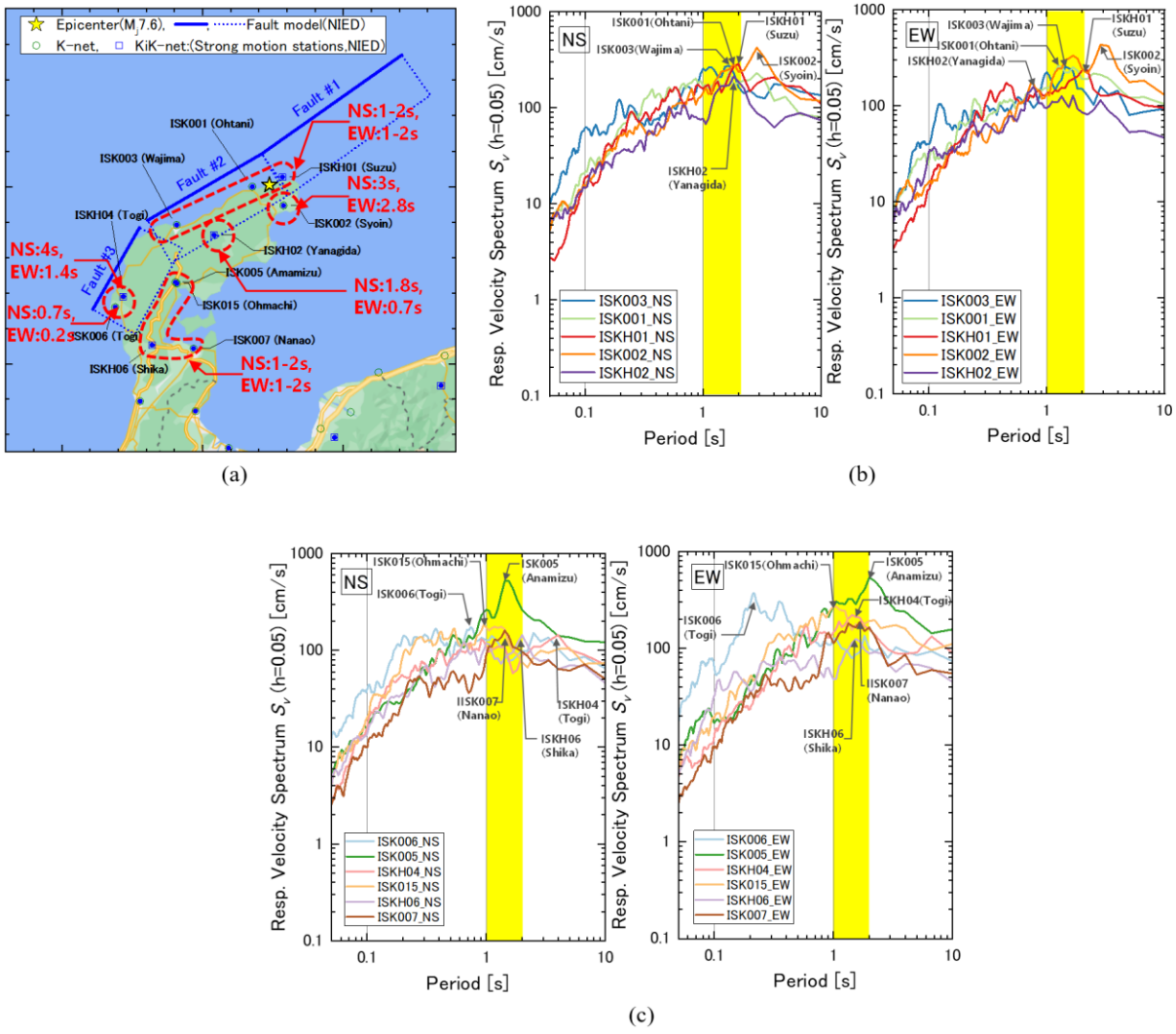

Figure 3.5. (a) Locations of analyzed K-NET and KiK-net stations with peak period ranges (b) Spectra for 5 stations near fault plane #2 (c) Spectra for 6 stations near fault plane #3

The stations K-NET Togi (ISK006) and KiK-net Togi (ISKH04), both situated directly above fault plane #3, exhibited distinct spectral characteristics despite recording high PGA values. ISK006 registered a PGA of 2820 Gal, while ISKH04 recorded 1220 Gal. At ISK006, both the NS and EW components showed a predominance in the short-period range, with the EW component reaching a response value of approximately 370 cm/s. In contrast, ISKH04 displayed dominant periods of 4 seconds for the NS component and 1.4 seconds for the EW component. The subsurface conditions at these sites differ significantly: ISK006 is underlain by 5 m of volcanic ash clay overlying bedrock, whereas ISKH04 features approximately 30 m of sandy clay. These variations in ground conditions likely contributed to the differences in spectral characteristics observed between the two sites.

Additionally, the large slip observed on fault plane #3, as illustrated in Figure 3.2, may have influenced the unique period characteristics in this region compared to other areas. The spectral features in this zone differ notably from those recorded elsewhere, primarily due to two factors: variations in local soil conditions and the proximity to the high-slip region on fault plane #3.

Figure 3.5(a) summarizes the peak period ranges of the velocity response spectra for all stations. A key characteristic of the mainshock ground motion was the concentration of peak periods in the 1–2 second range at many near-fault stations. However, significant variations in peak periods were evident across sites, reflecting differences in local site conditions and seismic wave propagation properties from each fault plane.

Stations near fault planes #2 and #3, in particular, exhibited divergent peak periods, which may have contributed to the spatial variability of damage patterns observed across the affected region. For example, areas where the predominant periods of ground motion coincided with the natural frequencies of local structures likely experienced amplified damage due to resonance effects. Further investigation is needed to establish correlations between these seismic motion characteristics and various forms of damage, including structural failures, landslides, and liquefaction phenomena.

4. General overview of the damage due to the earthquake

This section provides a summary of the damage caused by the 2024 Noto Peninsula Earthquake, as reported by the Cabinet Office of Japan (2024) as of 14:00 on August 21, 2024. The summary is based on the damage assessment methodology outlined by Ishii et al. (2024). The overview includes detailed accounts of the earthquake's impact across various sectors, encompassing human casualties, structural damage to buildings, disruptions to lifelines, damage to roads and transportation systems, and an estimation of the total economic loss.

4.1 Human casualties

Table 4.1 presents the distribution of human fatalities across the affected prefectures. Approximately 60% of the fatalities were attributed to crushing, suffocation, or respiratory failure resulting from building collapses or related incidents. The second most common cause of death was traumatic shock, accounting for around 10% of the fatalities, followed by hypothermia due to prolonged exposure to cold conditions, such as being trapped between collapsed structures and immobilized. Additional causes of death included burns, crush injuries, and cardiac arrest caused by prolonged compression.

Table 4.1. Number of human losses according to the (Cabinet Office of Japan, 2024).

Prefecture	Number of Human Losses			
	dead person	missing person	injured person	
			serious injury	minor injury
Niigata	2	0	8	44
Toyama	0	0	14	42
Ishikawa	339	3	335	876
Fukui	0	0	0	6
Nagano	0	0	0	0
Gifu	0	0	0	1
Aichi	0	0	0	1
Osaka	0	0	0	5
Hyogo	0	0	0	2
Total	341	3	357	977

4.2 Damage to buildings

Table 4.2 outlines the extent of building damage across various prefectures. Residential damage was most concentrated in Ishikawa, Niigata, and Toyama prefectures, with 6,273 buildings completely destroyed and 120,378 partially damaged. Additionally, 34,945 non-residential buildings were affected, and 17 fire-related incidents were reported exclusively in Ishikawa, Niigata, and Toyama prefectures. The damaged non-residential buildings included accommodation facilities, elder care facilities, centers for the disabled, facilities for children with disabilities, rescue centers, and child welfare facilities.

4.3 Damage to lifelines

Table 4.3 presents an overview of the damage to essential lifelines, including electricity, water, city gas, and telecommunications. According to the Ministry of Economy, Trade and Industry (METI), the peak number of power outages reached approximately 40,000 units. Between January 16 and January 31, efforts were made to improve access to affected areas, and outages were progressively resolved in regions where restoration was feasible. By this time, electricity had been fully restored, except for homes where safety concerns prevented reconnection. The Ministry of Land, Infrastructure, Transport, and Tourism reported that the maximum number of water supply disruptions was 137,000 units. As of July 30, all water outages had been resolved, except in areas where early restoration was challenging. METI further reported that municipal gas service was disrupted to 148 households due to pipeline damage caused by liquefaction; however, all gas services were restored by January 4 through recovery efforts. The maximum number of affected mobile stations was 839, with only 3 stations still out of service at present.

Table 4.2. Number of buildings damaged according to the (Cabinet Office of Japan, 2024).

Prefecture	Number of residential damage		Number of nonresidential damage	Number of fires
	Totally destroyed	Partially destroyed		
Niigata	108	21,980	65	2
Toyama	255	20,957	1,087	5
Ishikawa	5,910	76,657	33,783	11
Fukui	0	764	9	0
Nagano	0	20	0	0
Gifu	0	0	1	
Total	6,273	120,378	34,945	17

Table 4.3. Damage to lifelines (as of July 30, 2024).

Lifeline types	Damage	Restoration
Electric power	Maximum of 40,000 units without power	All restored
Water supply	Maximum of 137,000 water-cut off	Water outage resolved
City gas	Maximum number of stops 148	Resumption of supply
Mobile stations	Maximum number of stopped stations 839	3 suspended stations

4.4 Damage to roads and transportation networks

Ten expressway sections were closed to traffic due to road collapses, bridge damage, and surface deformations such as bumps and cracks. As of June 4, the Noetsu Highway remains closed, though all other highways have been restored. A section of the Directly Controlled National Highway was closed due to a landslide but has since been reopened. Forty sections of auxiliary national highways were closed due to landslides, subsidence, road damage, defective shoulders, damaged bridge supports, cracks in the road surface, and tunnel damage. As of July 30, 34 of these sections have been reopened, with 6 still closed. There were no reports of damage to the Shinkansen, and all lines resumed service by the afternoon of January 2. Five

conventional railway lines were suspended due to roadbed and rail damage; however, repairs have been completed, and all lines are now operational.

At Noto Airport, operations were temporarily suspended due to multiple cracks, each 10 cm deep and over 10 m long, in the runway. Following emergency repairs, commercial air service resumed on January 27. Ports and harbors generally continued operations as usual, except in the Noto area, where seven ports sustained damage to breakwaters and wharves, and six others experienced subsidence of their aprons due to liquefaction.

4.5 Estimated amount of damage

The Cabinet Office of Government of Japan has provided estimates for the economic impact of the Noto Peninsula Earthquake, ranging from approximately 1.1 trillion yen to 2.6 trillion yen (**Table 4.4**). These estimates are based on the damage rates in various sectors, including buildings and infrastructure such as electricity, water, and gas, with comparisons to previous earthquake data. By prefecture, the estimated damage for Ishikawa Prefecture is between 0.9 and 1.3 trillion yen, for Toyama Prefecture between 0.1 and 0.5 trillion yen, and for Niigata Prefecture between 0.1 and 0.9 trillion yen. Notably, the damage in Ishikawa Prefecture is particularly severe, accounting for 50-80% of the total. Regarding building damage, residential properties represent a significant portion, making up 35% of the total damage, with estimates ranging from 0.4 trillion yen to 0.9 trillion yen. When compared to the damage from past earthquakes, the impact of this event is estimated to be similar to that of the 2016 Kumamoto Earthquake and the 2007 Niigata Chuetsu-oki Earthquake, though it is less than the 16.9 trillion yen damage from the 2011 Great East Japan Earthquake and the 9.6 to 9.9 trillion yen damage from the 1995 Great Hanshin Earthquake.

Table 4.4. Estimated damage from the 2024 Noto Peninsula earthquake by the Cabinet Office (Trillion yen) (as of April 23, 2024) according to the method by (Ishii et al., 2024).

Item	2024 Noto Peninsula Earthquake M=7.6	2016 Kumamoto Earthquake M=7.3	2011 Great East Japan Earthquake M=9.0	2007 Niigata Chuetsu-oki Earthquake M=6.8	1995 Great Hanshin Earthquake M＝7.2
Building	0.6～1.3	1.6～3.1	10.4	0.7～1.2	6.3～6.5
Social infrastructure	0.5～1.3	0.4～0.7	2.2	0.3～1.2	2.2
Electric power, Water supply, Gas		0.1	1.3	0～0.1	0.5～0.6
Other social infrastructure		0.4～0.7	3	0.2～1	0.5～0.7
Total	1.1～2.6	2.4～4.6	16.9	1.7～3	9.6～9.9

5. Liquefaction in Ishikawa and Toyama Prefectures and its repercussions

5.1 Liquefaction in the area other than Uchinada Town

Liquefaction was observed in numerous areas during the 2024 Noto earthquake. In addition to the severe damage in the town of Uchinada, widespread liquefaction also affected Ishikawa, Toyama, and Niigata prefectures. This section outlines the liquefaction-related damage in Ishikawa and Toyama prefectures, excluding Uchinada town. Figure 5.1 presents a map of the cities discussed in this section.

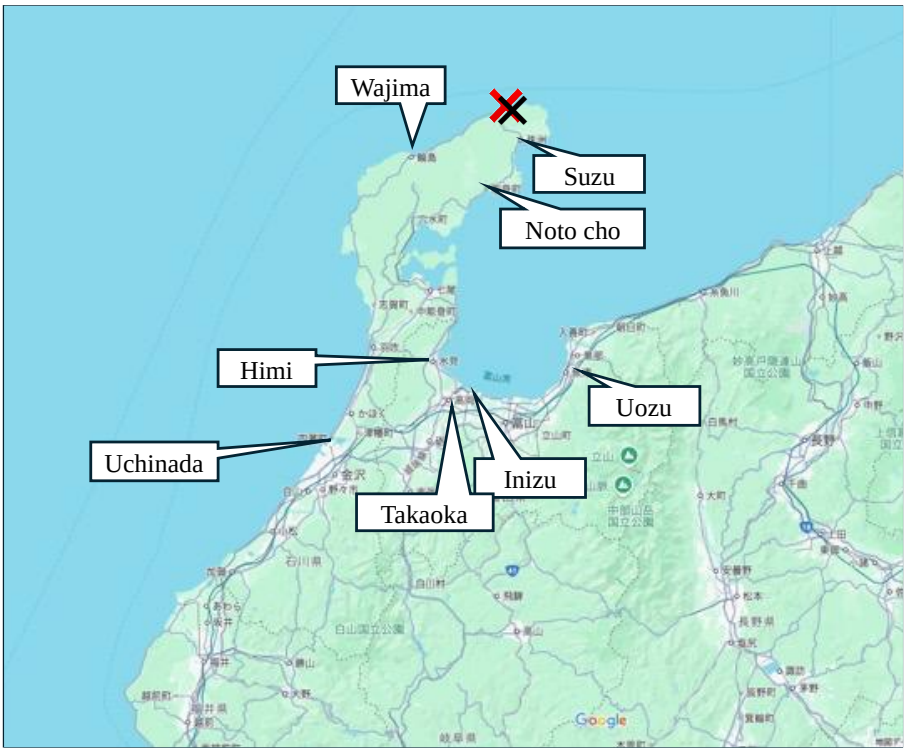

Figure 5.1. Map of Ishikawa and Toyama Prefecture.

5.2 Liquefaction in Ishikawa Prefecture

In Ishikawa Prefecture, significant liquefaction damage occurred in the northern region of the Noto Peninsula, particularly in the Okunoto area, in addition to the town of Uchinada. Earthquake induced damage was also severe in Suzu City, which experienced a seismic intensity of upper 6 on the Japanese seismic scale. The Ukai area was among the hardest-hit regions. As illustrated in Figure 5.2, numerous shafts were found to be nearly human-height, and many houses had their ground floors completely crushed, as shown in Figure 5.3. Typically, liquefaction damage to buildings results in gradual destruction. However, in the Ukai area, houses were immediately destroyed, suggesting that their collapse was caused by the intense shaking. Furthermore, as depicted in Figure 5.4, telegraph poles were tilted toward the sea, indicating that the buildings in this area may have been damaged by the undertow generated by the receding tsunami during the earthquake. It is believed that the Ukai area

suffered extensive damage due to the combined effects of liquefaction, strong seismic shaking, and the tsunami-induced rip currents.

Figure 5.2. Liquefaction causes manholes lifting phenomenon (Suzu City, Ishikawa Prefecture). Lat: 37.40073°, Lon: 137.24304°

Figure 5.3. Detached house collapsed due to multiple factors (Suzu City, Ishikawa Prefecture). Lat: 37.40178°, Lon: 137.24284°

Figure 5.4. A utility pole leaning toward the sea (Suzu City, Ishikawa Prefecture). Lat: 37.39912°, Lon: 137.24358°

In contrast, in Wajima City, where the earthquake's magnitude was similar to that in Suzu City, liquefaction damage was not as severe. Similar to Pearl City, the shafts were raised by liquefaction, but the height of the shafts above the ground was approximately half the height of a human body, as shown in Figure 5.5. In Wajima City, damage also occurred due to the uplift of the seabed in the harbor and along the coastline, along with a fire at the morning market.

Figure 5.5. Liquefaction causes manholes lifting phenomenon (Wajima City, Ishikawa Prefecture). Lat: 37.39358°, Lon: 136.91582°

In Noto Town, where the earthquake intensity was comparable to Suzu City, uneven subsidence and lateral flow due to liquefaction were observed at Uizu Port, as shown in Figure 5.6. Additionally, Figure 5.7 shows that roads surrounding private homes near Uizu Port were covered with sand from sand eruptions caused by liquefaction. While several houses collapsed,

it is believed that the collapse was primarily due to the intense shaking of the earthquake rather than liquefaction itself.

Figure 5.6. Liquefaction at the Port of Uitsu (Noto Town, Ishikawa Prefecture). Lat: 37.30639°, Lon: 137.15124°

Figure 5.7. Liquefaction around private houses near Uitsu Port(Noto Town, Ishikawa Prefecture). Lat: 37.30706°, Lon: 137.15016°

5.3 Liquefaction in Toyama Prefecture

In Toyama Prefecture, liquefaction was observed in several coastal areas, with the western part of the prefecture experiencing an intensity of 5+ on the Japanese seismic scale.

In Imizu City, extensive liquefaction was observed in the Shinminato area. Sand eruptions, ranging from 80 cm to 2 meters in diameter, were seen at multiple locations, as shown in Figure 5.8. Fountain marks, indicative of liquefaction, were also observed alongside the sand eruptions, as seen in Figure 5.9. At Shinminato Fishing Harbor, subsidence caused by liquefaction and other factors disrupted the functioning of the harbor, as shown in Figure 5.10. A similar situation occurred at Fushiki Port in Takaoka City, where substantial sand fountains emerged, and numerous instabilities due to liquefaction were observed, impairing logistics and daily activities, as depicted in Figure 5.11. In Takaoka City, liquefaction damage was widespread in both inland and coastal areas (Figure 5.12), with most damage believed to have occurred in the vicinity of the old river channel.

Figure 5.8. Sand eruption site in Shinminato, Toyama Prefecture, Japan (Imizu City, Toyama Prefecture). Lat: 36.78020°, Lon: 137.10301°

Figure 5.9. After fountain caused by liquefaction (Imizu City, Toyama Prefecture). Lat: 36.78097°, Lon: 137.09959°

Figure 5.10. Damage to Shinminato Fishing Port due to liquefaction (Imizu City, Toyama Prefecture). Lat: 36.78250°, Lon: 137.09720°

Figure 5.11. Liquefaction damage on a road in Toyama Fushiki Port (Takaoka City, Toyama Prefecture). Lat: 36.80089°, Lon: 137.06691°

In Himi City, located closest to Ishikawa Prefecture, severe liquefaction damage was observed in the Shindo area. Similar to other affected regions, widespread sand eruptions were seen, and the city experienced significant damage, such as house tilting due to uneven settlement and delays in the restoration of the water supply caused by liquefaction, as shown in Figures 5.13 and 5.14.

Liquefaction was also observed in Uozu, in the eastern part of Toyama Prefecture, where an intensity of 4 was recorded. Partial sand eruptions were observed in car parks and on roads near Uozu Fishing Port (Figure 5.15). However, the damage in this area was relatively minor

compared to that in western Toyama Prefecture, likely due to the lower intensity of the earthquake in this region.

Figure 5.12. Liquefaction damage in old river channel (Takaoka City, Toyama Prefecture). Lat: 36.75944°, Lon: 137.00375°

Figure 5.13. Damage to gutters due to liquefaction (Himi City, Toyama Prefecture). Lat: 36.87181°, Lon: 136.98319°

Figure 5.14. A house that deflects from side to side due to immobile subsidence caused by liquefaction (Himi City, Toyama Prefecture). Lat: 36.86425°, Lon: 136.98546°

Figure 5.15. Sediment eruption at Uozu Fishing Port (Uozu City, Toyama Prefecture). Lat: 36.82440°, Lon: 137.39305°

5.4 Liquefaction in Ishikawa Prefecture (Uchinada Town and Kahoku City)

In the area extending from Ōhsaki in Kahoku City to Miyasaka in Uchinada Town (Figure 5.16), significant ground deformation has been observed, particularly along the base of the sand dune slopes near Prefectural Road 8, where it occurs in a continuous, belt-like pattern. Soil liquefaction has led to the formation of sand boils, resulting in uneven settlement and ground uplift, which has caused numerous buildings to tilt or sink. In addition, retaining walls have collapsed or shifted, road pavements have been damaged and raised, and utility poles have

tilted noticeably. Blockages in waterways have also been observed in some areas. Many residents have been forced to evacuate homes that were rendered uninhabitable. Figures 5.17-5.20 illustrate examples of the ground deformation and associated damage.

Our investigation revealed a pattern of ground subsidence and uplift occurring simultaneously, characterized by multiple parallel subsidence lines, interpreted as tension cracks. Uplift has occurred on the lower side of these subsidence lines (on the reclaimed land side), forming along the compression axis in the same direction as the slope of the ground. Above the subsidence lines (on the sand dunes side), ground deformation is minimal. Notably, between the subsidence and uplift zones, there are prominent features such as sand boils, ground settlement, and tilting of structures. The compression axis of the tension cracks and uplift aligns in a northeast-southwest direction along the dune ridge. Based on these observations, it can be concluded that the subsidence and uplift resulted from ground failure induced by lateral movement due to liquefaction.

An example of ground deformation caused by lateral movement at Sakakibara Shrine in Ōhsaki, Kahoku City, is shown in Figure 5.21, along with a schematic cross-section. This deformation appears to have been caused by a slope failure resulting from lateral flow on a gently sloping area with a gradient of approximately 3 degrees and a height difference of around 2 meters. Interestingly, Prefectural Road 8, located at the base of the slope, did not collapse due to the lateral flow induced by liquefaction. Instead, the road effectively prevented the flow from the west side and was uplifted due to compression, experiencing horizontal bending in several locations.

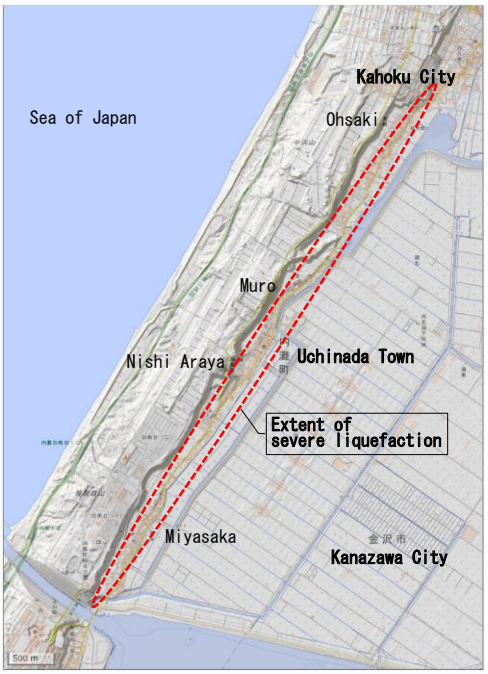

Figure 5.16. Area affected by severe soil liquefaction

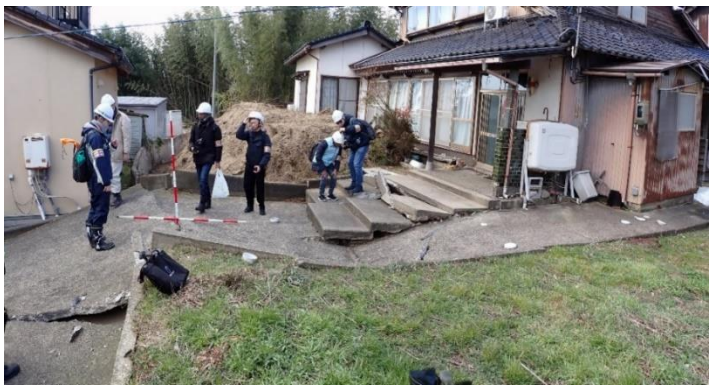

Figure 5.17. Damage in the Ohsaki area of Kahoku City (Uplift of road and lateral movement of houses). Lat: 36°42'23.62", Lon: 136°41'27.08"

(a) (b)

Figure 5.18. (a) Blockage of water channel due to liquefaction-induced lateral spreading. Lat: 36°41'30.8", Lon: 136°40'51.4" (b) 12 m lateral displacement experienced by a residential building owing to lateral spread. Lat: 36°41'32.43", Lon: 136°40'49.62"

(a) (b)

Figure 5.19. (a) Pile supported undamaged house in Muro. Lat: 36°41'31.58", Lon: 136°40'50.06" (b) Differential settlement for a building with shallow foundation in Miyasaka. Lat: 36.67329°, Lon: 136.66323°

(a) (b)

Figure 5.20. (a) Subsidence of the Nishi Araya school building. Lat: 36°40'42.25", Lon: 136°40'3.53" (b) Uplifting of the road. Lat: 36°40'37.89", Lon: 136°40'2.71"

(a) Area location

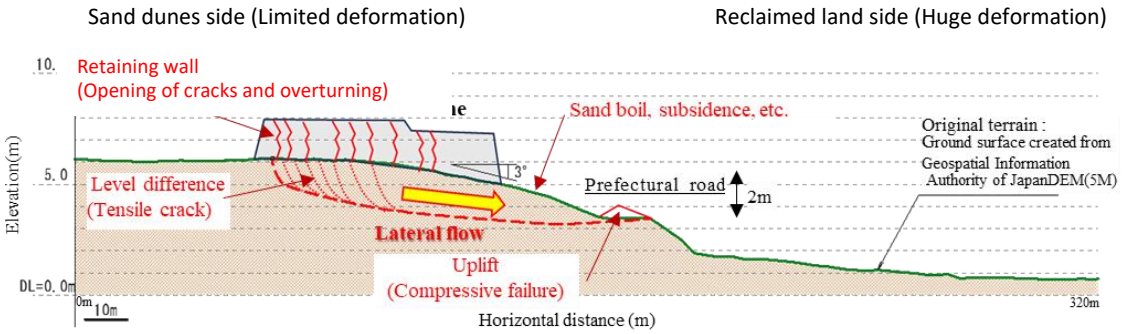

(b) Schematic cross section

Figure 5.21. Liquefaction-induced lateral spreading along the Sakakibara shrine located in Ohsaki area (Kahoku City)

The preliminary reconnaissance survey conducted by the authors on February 3 and 4, 2024 (approximately one month after the disaster) revealed significant deformations in several geotechnical and structural systems in the Nishi Araya area, located south of Muro. The primary cause of these large deformations was liquefaction-induced lateral spreading, which resulted in widespread ground failure throughout the area, accompanied by the ejection of sand. Figure 5.22 illustrates a typical example of ground surface settlement caused by lateral spreading.

Figure 5.22. Settlement of the ground surface adjacent to the Prefectural Road 8. Lat: 36°40'41.70", Lon: 136°40'4.36"

Our initial investigation revealed that the effects of liquefaction-induced lateral spreading were most pronounced on the lower side of the Uchinada sand dunes, toward Prefectural Road 8. Figure 5.23 provides a view of the damaged Prefectural Road 8, highlighting severely tilted utility poles and buildings.

Figure 5.23. Significant uplift of the left side of Prefectural Road 8 with tilted poles clearly visible. Lat: 36°40'41.64", Lon: 136°40'4.80"

Figure 5.24. Close-up view of the building's compound wall tilted towards Prefectural Road 8. Lat: 36°40'42.03", Lon: 136°40'5.18"

Figure 5.25. Significant tilting of the entrance staircase towards Prefectural Road 8. Lat: 36°40'43.99", Lon: 136°40'6.88"

The uplift of the road pavement due to liquefaction-induced lateral spreading is clearly visible. The lateral spreading occurred in the direction of the reclaimed land, exerting a substantial lateral thrust on the utility poles, buildings, and other infrastructure in the vicinity, causing them to tilt significantly toward the reclaimed land. Figures 5.24 and 5.25 provide close-up views of two buildings that sustained severe damage, with the compound walls and staircases tilted toward Prefectural Road 8 as a result of the considerable lateral thrust applied. Figure 5.26 illustrates the collapse of a parking shed caused by lateral spreading, accompanied by notable sand ejecta.

Figure 5.26. Collapse of the parking shed. Lat: 36°40'43.62", Lon: 136°40'6.50"

Figure 5.27 depicts the subsidence and multiple cracks observed at the entrance of Nishi Araya Elementary School. Additionally, the school's playground sustained significant damage, with a visible crack line leading to shear rupture of the ground, as shown in Figure 5.28.

Figure 5.27. Damage to the entrance of Nishi Araya elementary school. Lat: 36°40'42.25", Lon: 136°40'3.53"

Figure 5.28. Observation of tension cracks at the playground of Nishi Araya elementary school. Lat: 36°40'44.83", Lon: 136°40'2.33"

A significant vertical displacement of approximately 500 mm was observed between the two sections of the failed ground, as shown in Figure 5.29.

Figure 5.30 illustrates some of the lateral flow induced damage in the Muro district. On the gentle slope on the Kahoku lagoon side of Prefectural Road 8, lateral flow was observed, which resulted in the blockage of the waterway. In the vicinity of Prefectural Road 8, a subsidence zone developed, characterized by stepped subsidence and open cracks.

Figure 5.29. Formation of a vertical gap of 50 cm between the two ruptured parts of the ground. Lat: 36°40'44.64", Lon: 136°40'2.11"

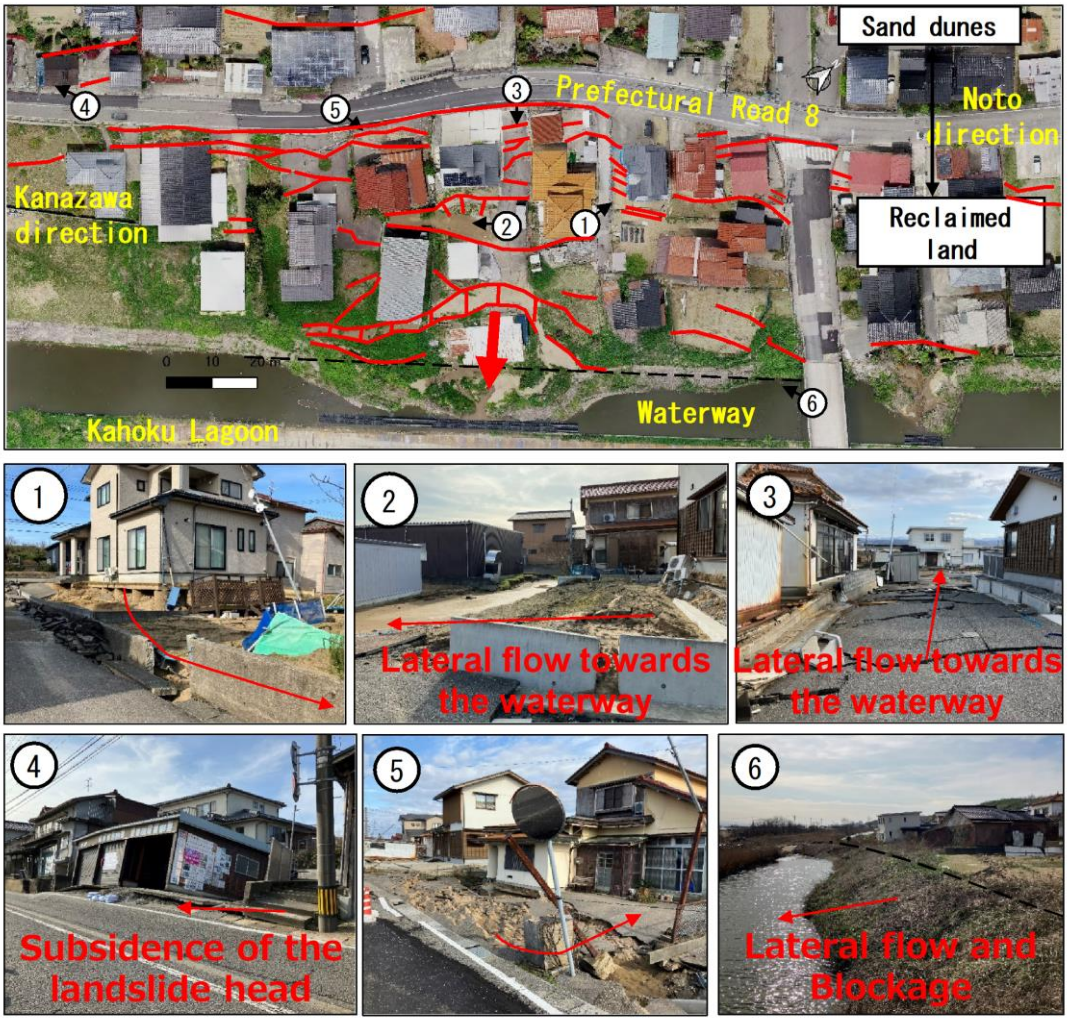

Figure 5.30. Lateral Flow induced damage in Muro district.

6. Topography, Geology and History of Reclamation in Uchinada Town, Ishikawa Prefecture

Coastal sand dunes extend along the coastline of the Kaga region in Ishikawa Prefecture, from the Komatsu Plain in the south to the northern reaches of the area. These dunes are sequentially distributed as follows: the Daishoji Dunes, the Komatsu Dunes, the Yasuhara Dunes, and the Uchinada Dunes (Fuji, 1971). The Uchinada Dunes, classified as transverse dunes, span approximately 1.5 km in width, stretching from Awagasaki Town in Kanazawa City to Hidono in Kahoku City. The dunes reach a maximum elevation of 60 meters, with an average height of 20 meters. Their seaward slopes are gentle, while the inland slopes are steep, as shown in Figure 6.1.

The region extending from Ohsaki in Kahoku City to Miyasaka in Uchinada Town lies on the southeastern side of the dunes (the reclaimed land side). The sand dunes in this area are aligned in a northeast-southwest direction, with an elevation of about 50 meters. The land here was once part of the brackish Kahoku Lagoon, where small-scale land reclamation began during the Edo period. Large-scale reclamation was initiated under the National Kahoku Lagoon Land Reclamation Project in 1963, and the land was fully reclaimed by 1971. During this reclamation, substantial excavation of the dune sands took place, and according to historical topographic maps, areas that were once dune slopes were transformed into flat residential land, as depicted in Figure 6.2.

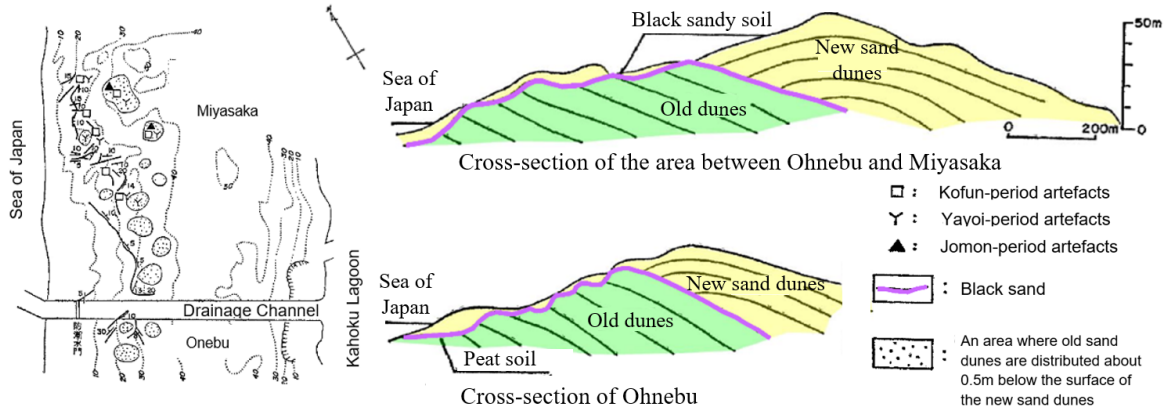

Figure 6.1. Cross sectional view of Uchinada sand dunes (After Fuji, 1971).

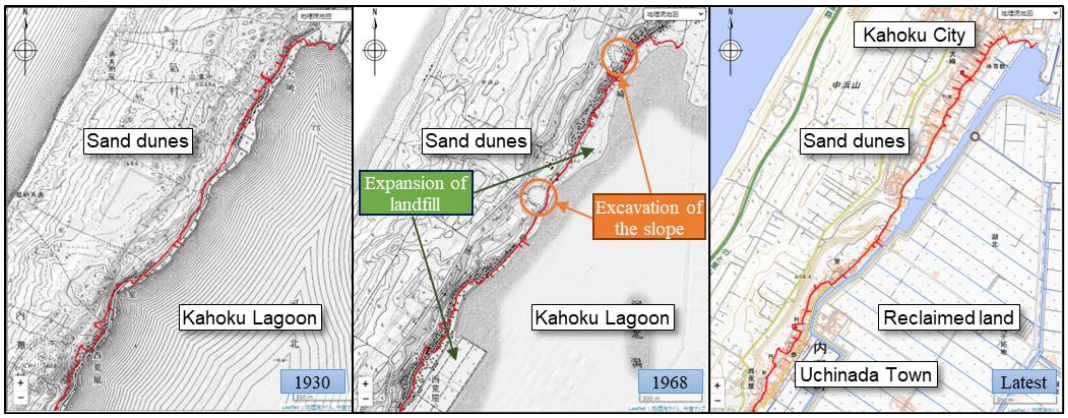

Figure 6.2. Topographic change from Ohsaki (Kahoku City) to Miyasaka (Uchinada Town).

7. Remote Sensing and Field Testing in the Liquified Area

7.1 Location of the Surveyed Area

To assess the geological and geotechnical characteristics, as well as the liquefaction potential of the area, ground investigations were carried out in the Nishi Araya and Muro districts of Uchinada Town (Figure 7.1), where significant liquefaction and lateral flow-induced damage were observed during our preliminary survey.

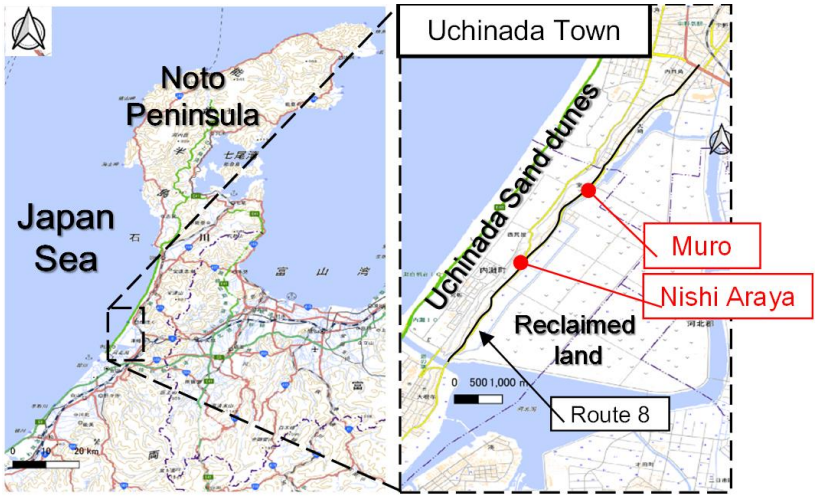

Figure 7.1. Surveyed area

Figure 7.2. Aerial photograph (before and after land reclamation) of the Nishi Araya area (After Tani, 2016)

The survey site in the Nishi Araya area is situated at the edge of the Uchinada sand dunes (Figure 7.2). This location was excavated for sand extraction during the 1960s following the reclamation of the former Kahoku Lagoon and was subsequently filled in during the 1970s, a condition that persists to the present day. Nishi Araya Elementary School, located in the area, sustained severe damage due to liquefaction and remains closed. Based on historical aerial photographs, land records, and geological survey results, it has been determined that the area between Nishi Araya Elementary School, which experienced significant liquefaction damage, and Prefectural Road 8 (indicated by the red line in Figure 7.3) contains a reclaimed layer extending to a depth of approximately 7 meters.

Additionally, a borehole investigation conducted in August 2023, prior to the disaster, revealed that the reclaimed layer (Fs) extends from the surface to a depth of approximately 7.0 meters (Figure 7.3). Beneath this layer, a dune layer (Sd) was identified from 7.0 to 10.0 meters,

followed by an alluvial sand layer (As) from 10.0 to 11.3 meters, an alluvial clay layer (Ac) from 11.3 to 27.6 meters, and a diluvial sand layer (Ds) from 27.6 to 33.45 meters.

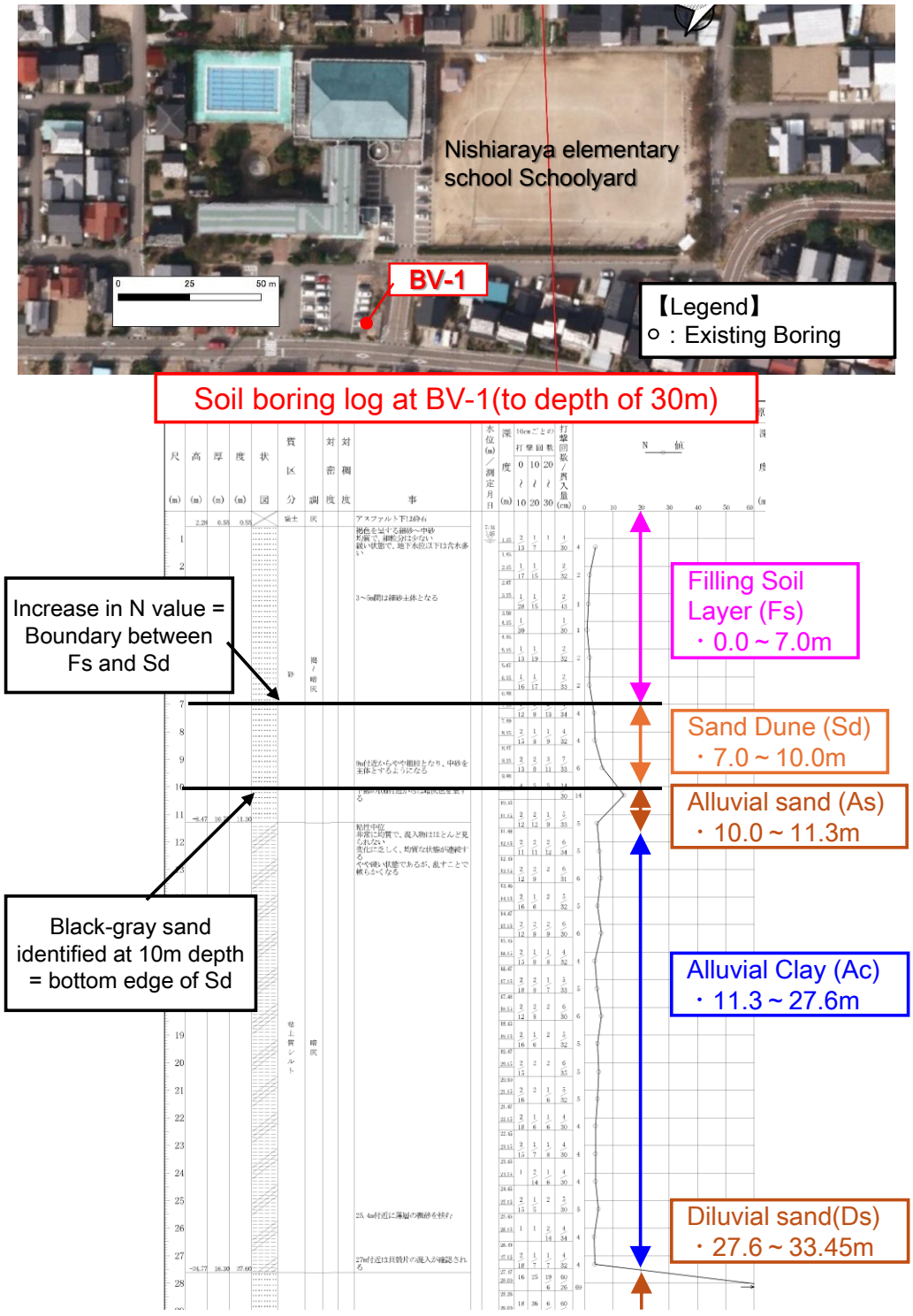

Figure 7.3. Borehole investigation result near the Nishi Araya elementary school

The Muro area is situated at the edge of the Uchinada sand dunes and is believed to have been reclaimed following the installation of waterways during the reclamation of the former Kahoku Lagoon (Figure 7.4). Analysis of historical aerial photographs, land records, and geological survey results revealed the presence of a reclaimed layer extending from 1.5 to 4.5 meters in

depth within this region (Figure 7.5). Significant liquefaction and lateral flow-induced damage were observed in the area to the east of Prefectural Road 8. A borehole investigation conducted by the authors after the disaster (Figure 7.5) confirmed the presence of a reclaimed layer (Fs) extending from the surface to a depth of 4.5 meters, a dune layer (Sd1) from 4.5 to 6.7 meters, and an alluvial clay layer (Ac) from 6.7 to 9.5 meters.

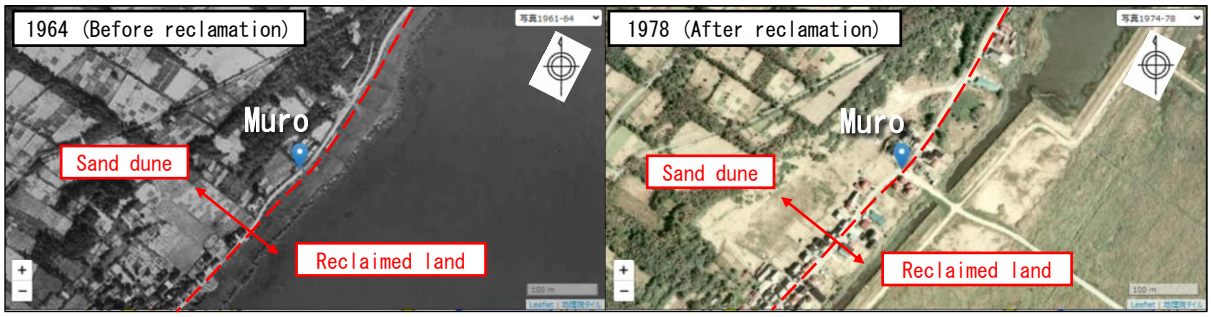

Figure 7.4. Aerial photograph (before and after land reclamation) of the Muro area (After Tani, 2016)

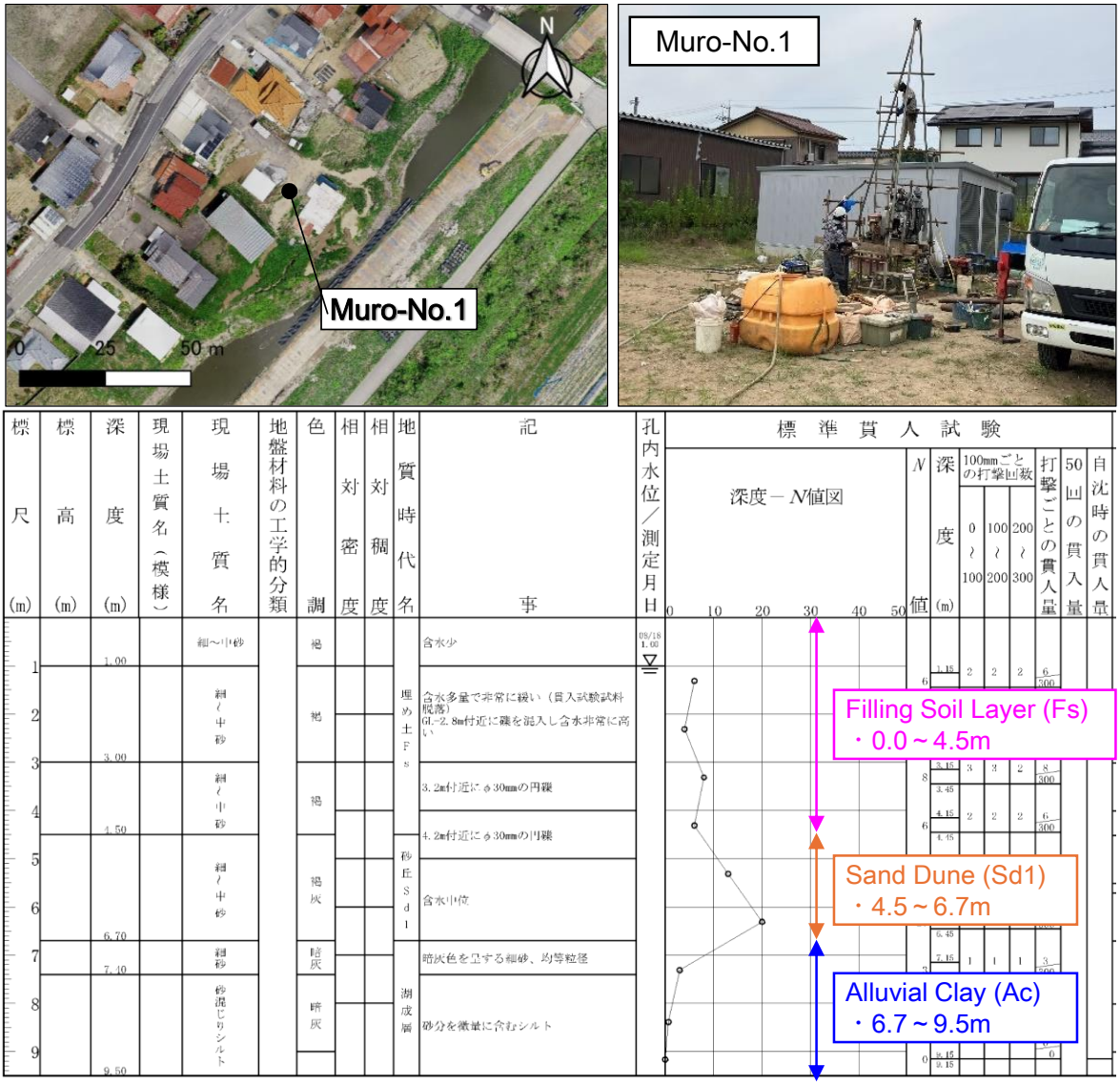

Figure 7.5. Geological survey in Muro district

Figure 7.6 presents the results of the grain size analysis for samples collected from the top of a dune (Sample No. 1) and from sand boiling sites (Samples No. 2 to No. 7).

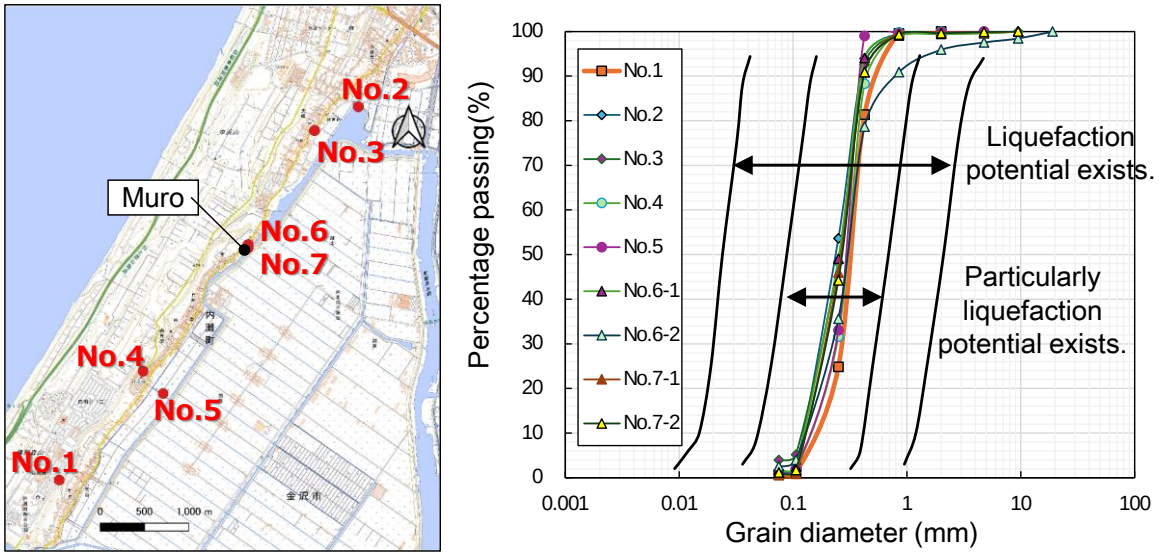

Figure 7.6. Results of grain size analysis for samples collected in Uchinada Town

Table 7.1 summarizes the typical geotechnical features observed at each sampling location post-disaster. The grain size distributions of the samples from both the dune and the sand boiling sites are generally similar, with both locations classified as sands exhibiting characteristics that suggest a high potential for liquefaction.

Table 7.1. List of sampling sites for grain size analysis

No.	Sampling sites
1	・Sand dune (no liquefaction damage)
2	・Sand boiling location
3	・Sand boiling location
4	・Nishi Araya elementary school ground
5	・Sand boiling location
6	・Muro district residence (house with ground improvement piles)
7	・Muro district residence (house moved 12 meters)

8. Case Studies on Liquefaction and Lateral Flow

8.1 Investigation Methods

The following remote sensing and in situ investigations were conducted in the Nishi Araya and Muro areas, where significant damage to low-rise buildings was observed due to lateral flow. The objectives of each survey technique are outlined below:

- UAV Photogrammetry (Nishi Araya only) and 3D Laser Scanning: Used to conduct precise surveys over a wide area to assess post-liquefaction ground deformation.
- Portable Dynamic Cone Penetration Test (PDCPT): Enables continuous assessment of soil hardness and softness during testing.
- Screw Driver Sounding (SDS) Test: Measures rotational torque and applied load during ground penetration, allowing for the classification of soil layers and preliminary identification of soil types (Tanaka et al., 2014).
- Piezo Drive Cone (PDC) Test: Measures pore water pressure through dynamic penetration and estimates the N-value and fine content (FC) to evaluate the soil's liquefaction resistance (PDC Consortium, Japan).
- Surface Wave Exploration (Muro only): A geophysical technique for investigating shallow subsurface structures by analyzing surface waves (Rayleigh waves) generated by hammer impacts on the ground surface (Hayashi et al., 2001).
- Standard Penetration Test (SPT): Conducted in Muro only, this standard method provides insights into soil density and strength.

8.2 Case Study 1: Field Survey and Results for the Nishi Araya Area

8.2.1 UAV Photogrammetry and 3D Laser Scanner

Figure 8.1 illustrates the field survey locations in the Nishi Araya area. The yellow circles indicate the locations of the conducted surveys, while the blue circles denote the positions of the existing boring surveys.

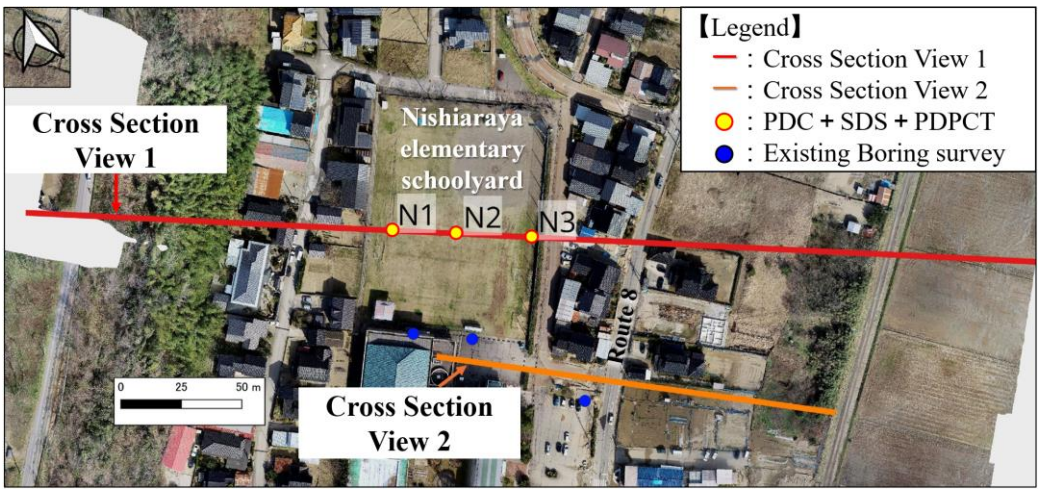

Figure 8.1. Selected locations for the field survey in Nishi Araya area

Figure 8.2 presents the 3D point cloud data derived from UAV photogrammetry along with the field survey results from the Nishi Araya area. The UAV photogrammetry identified several key features, including crack patterns on the playground of Nishi Araya Elementary School (denoted by red lines), lateral displacement of houses (indicated by red ellipses), and deformation along Prefectural Road 8 (highlighted by a blue ellipse), all of which were also observed during the field survey. Furthermore, the crack line was found to coincide with the location of the excavation site, which was later filled during the reclamation process, as shown in Figure 8.2.

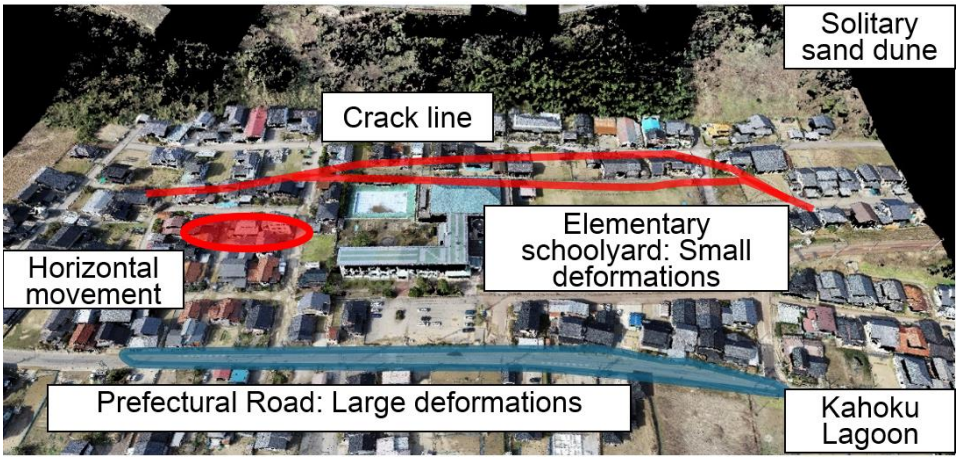

Figure 8.2. Deformation pattern observed in Nishi Araya area following the UAV surveying

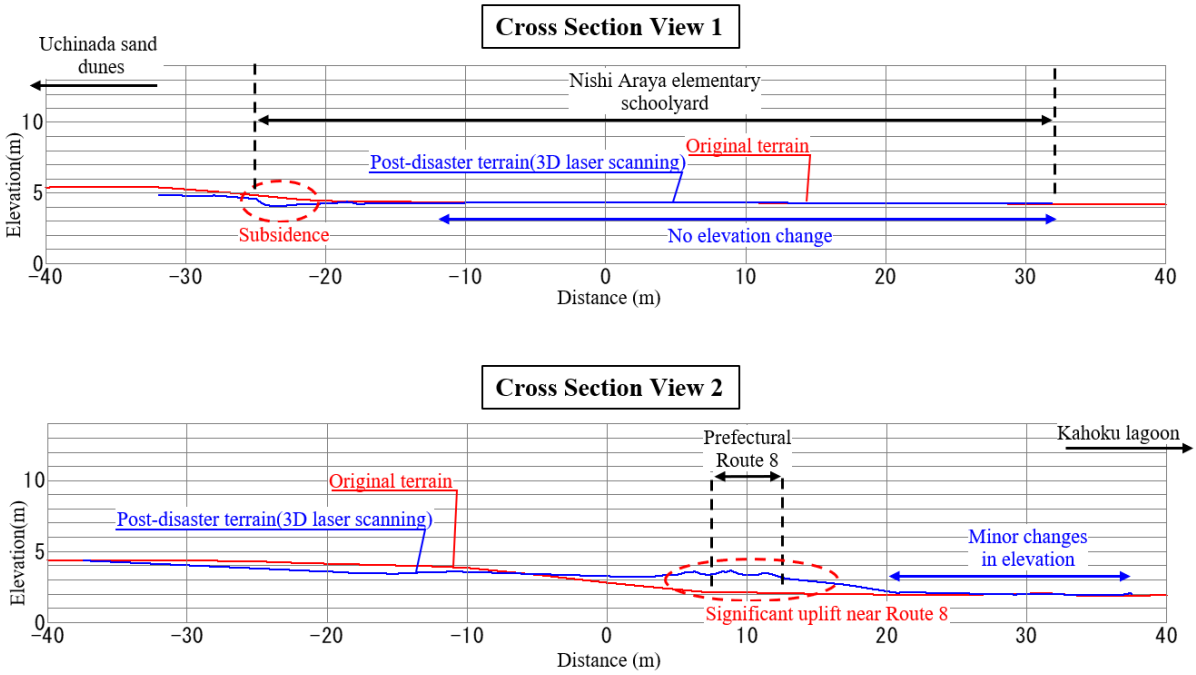

Figure 8.3. Comparison between the pre-disaster and post-disaster terrain (3D laser scanning)

Figure 8.3 presents a comparison between the pre-disaster topography (5m mesh DEM data from October 5, 2016, obtained from GSI, Japan) and the post-disaster topography (remote

sensing data from February 4, 2024) collected through our 3D laser scanner survey, for the two cross-sections (1 and 2) near Nishi Araya Elementary School, as shown in Figure 8.1. In cross-section 1, subsidence is evident at the playground of Nishi Araya Elementary School (on the Uchinada sand dunes side), where cracks had formed. However, no change in elevation was observed from the center of the playground to the side of Prefectural Road 8. In contrast, cross-section 2 shows significant uplift near Prefectural Road 8, with no major topographical changes detected in the paddy field area toward Kahoku Lagoon.

8.2.2 Portable Dynamic Cone Penetration Test (PDCPT) Tests

To gain further insight into the characteristics of liquefied sand following the earthquake, PDCPT was performed. Figure 8.4 illustrates the three locations within the playground of Nishi Araya Elementary School that were selected for the PDCPT analysis.

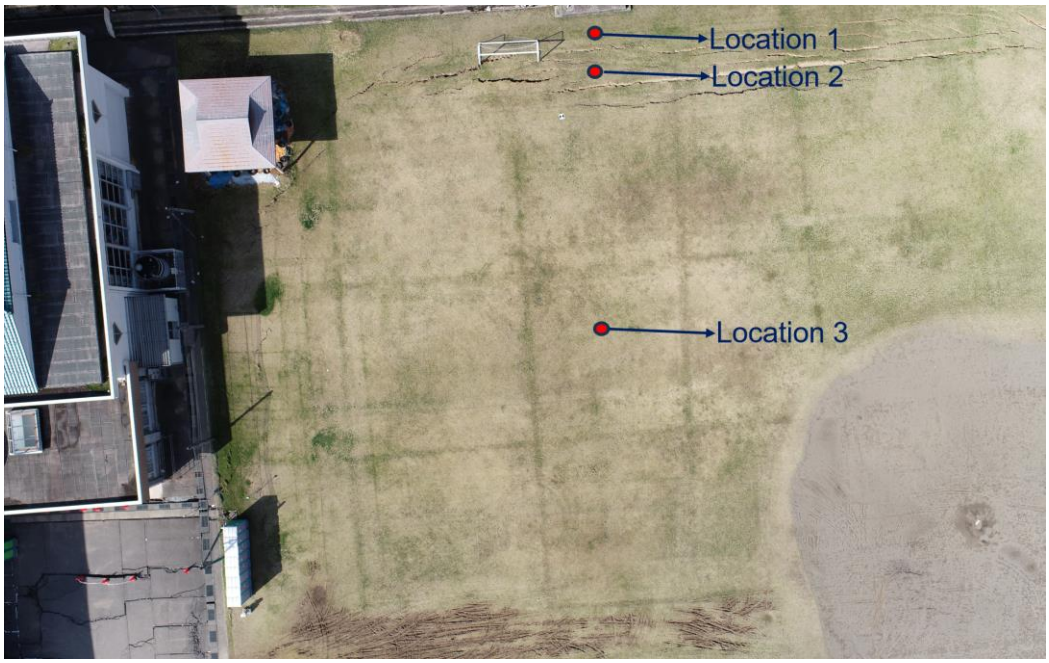

Figure 8.4. Drone view of the three locations (located at the playground of Nishi Araya elementary school) selected for portable dynamic cone penetration testing

These locations were selected along the direction of lateral spreading for the PDCPT testing, which was conducted in accordance with the guidelines established by the Japanese Geotechnical Society (JGS). The data obtained from the PDCPT tests are crucial for conducting ground response analyses, understanding the propagation mechanism of cyclic stresses with depth, and ultimately clarifying the mechanisms behind lateral spreading and the extensive nature of soil deformations. During the PDCPT testing, the number of blows, denoted as Nd, was initially recorded. This Nd value was subsequently converted to the SPT-N value following the procedure recommended by Takase and Sasada (2013), using the set of equations outlined in their methodology.

$$N_d < 4, N = 1.1 + 0.3N_d \quad (1)$$

$$N_d > 4, N = 0.66N_d \quad (2)$$

Figure 8.5 presents the converted SPT N-value profiles along the penetration depth for the three locations. It is evident that the soil is extremely soft, with estimated SPT N-values consistently below 10 throughout the 5-meter penetration depth. Notably, there is a decrease in the SPT N-value as the penetration depth approaches 5 meters at all three locations, indicating that the soil becomes relatively looser under increased confining stress. This suggests that, under cyclic loading, the loose bottom layer is highly susceptible to liquefaction.

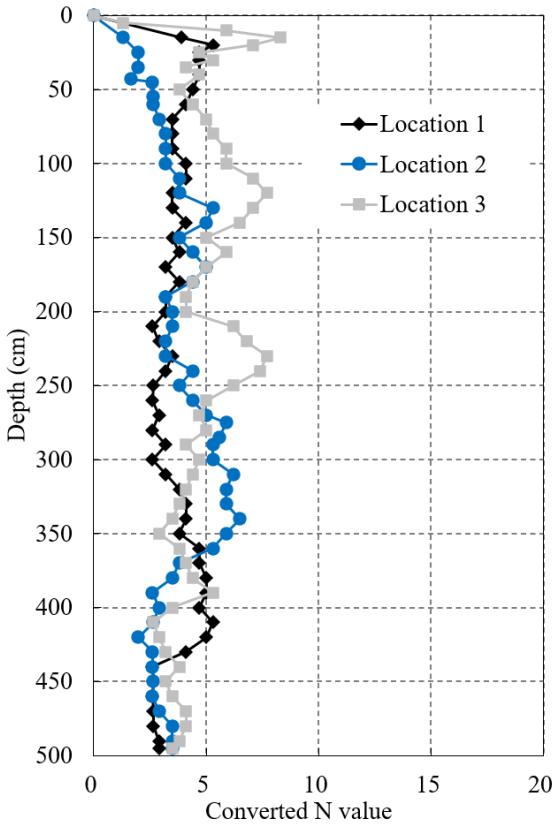

Figure 8.5. Converted N value along the depth

8.2.3 Screw Driver Sounding (SDS) Tests

In the SDS testing, the rotational load is increased by 125 N per rotation for every 25 cm of elevation, up to a maximum of 1 kN. During the tests, the applied load, rotational torque, settlement speed, and total settlement were measured. The torque was recorded by rotating the rod at 25 cm intervals, with the rod being raised by 2 cm after each rotation. Assuming that the rotational speed of the rod reflects the combined shear, the circumferential friction force acting on the rod was calculated. The corrected torque and load acting on the screw point were then determined by subtracting the components of circumferential friction (both rotational and vertical) from the measured values.

The relationship between the corrected torque and load indicates that, for sandy soils, the torque value increases nearly proportionally with depth. Conversely, for cohesive soils, the torque remains relatively constant despite an increase in vertical load. These trends in the corrected torque profile with depth can be used to classify the soil strata. Furthermore, by correlating the

results from the Screw Driver Sounding test with the Standard Penetration Test (SPT), the N-value can be estimated based on the penetration energy for a 25 cm depth.

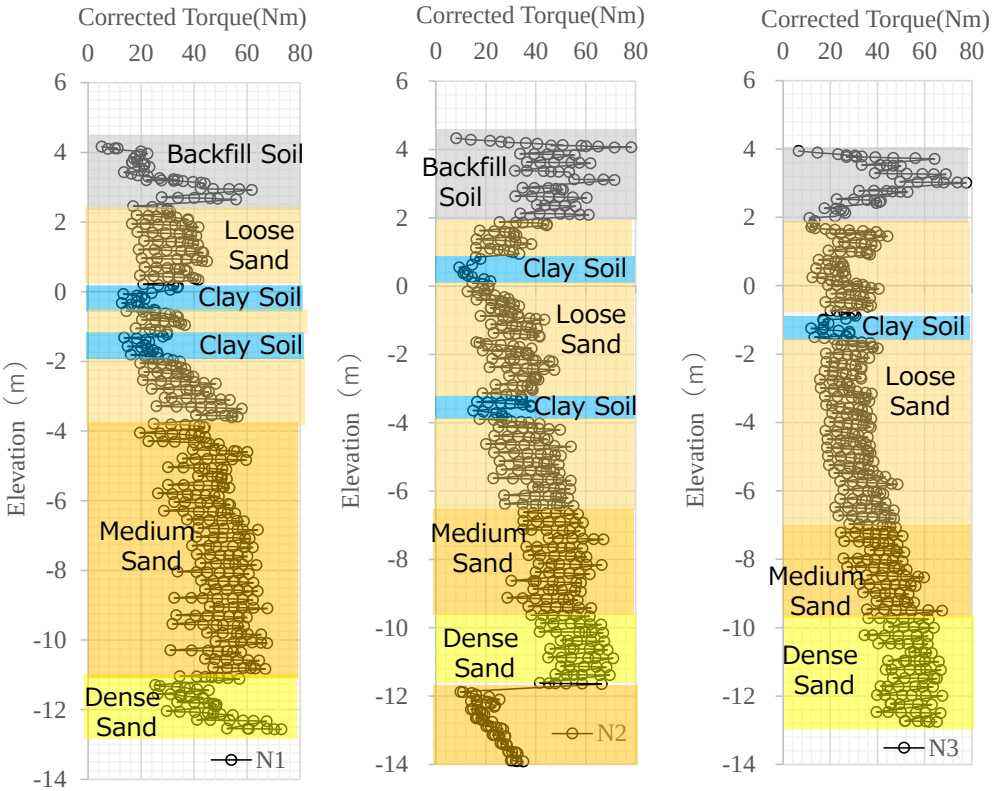

Figure 8.6. Relationship between corrected torque and elevation

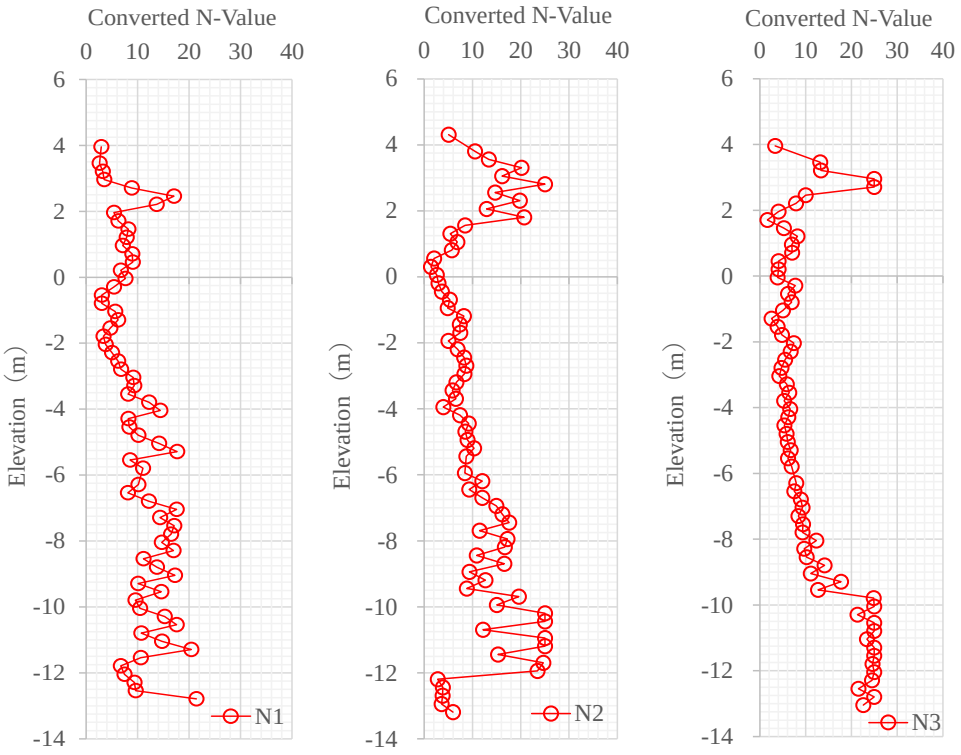

Figure 8.7. Relationship between converted N value and elevation

Figures 8.6 and 8.7 present the relationship between corrected torque and elevation, and the correlation between the converted N-value and elevation at each survey site, respectively. At the N1 site, the corrected torque values near the surface are smaller than those observed at other survey sites. From the SDS test results, it was determined that the soil at N1 is clayey at elevations of 0 m and 1 m. At the N2 site, a clay layer was identified at an elevation of -3 m, while at N3, the clay layer is present at -1 m. The smaller increase in corrected torque near the surface (i.e., above -1.5 m) suggests that the soil is sandy with a high fine-grained content. The estimated N-value at -11 m is less than 10, while at -14 m it exceeds 20, indicating that the depth range between -11 m and -14 m consists of dense sand, although slight differences exist among the N1, N2, and N3 sites.

8.2.4 Piezo Drive Cone (PDC) Tests

PDC test is a method used to assess the soil's hardness and softness, as well as to classify its grain composition (fine-grained content, Fc). This is achieved by measuring the excess pore water pressure (Δu) during impact penetration, using a pore water pressure meter integrated into the tip of the dynamic penetration test cone. The penetration resistance (Nd) obtained from this test corresponds to the N-value of the Standard Penetration Test (SPT) conducted during borehole investigations. Additionally, the fine-grained content (Fc) can be estimated from the response of the pore water pressure in the ground, specifically through the pore water pressure ratio (uR/σ'v).

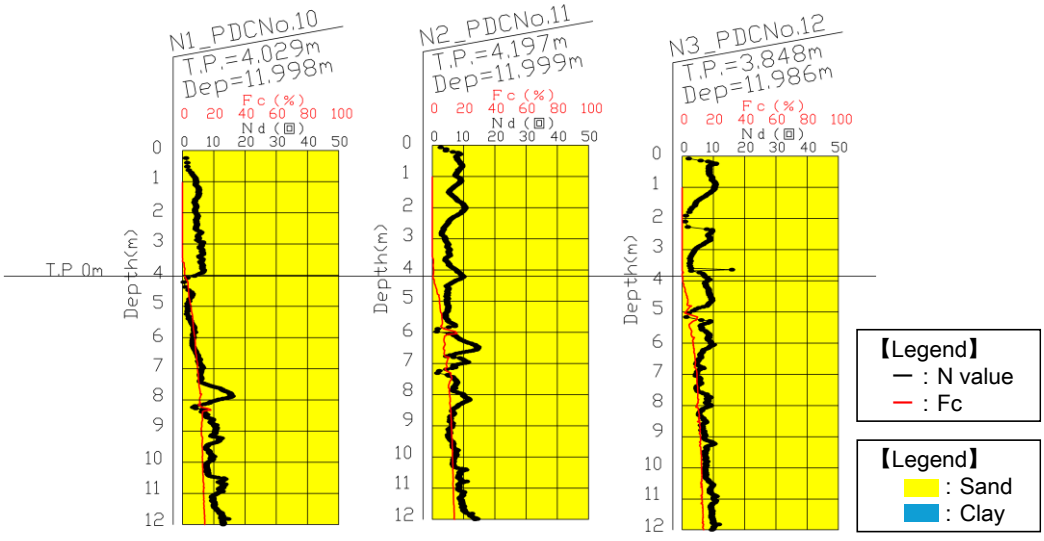

Figure 8.8. Depth profiles of fine grain content Fc based on PDC test (Nishi Araya area)

Soil classification using the PDC test indicated the presence of a loose sandy layer with a fine-grained content (Fc) of less than 10% and an Nd value of less than 10, extending to a depth of 12 meters, as shown in Figure 8.8.

8.2.5 Comparison of the Sounding Test Results

Figure 8.9 presents the depth profiles of the equivalent N-values and fine content (Fc) at location N1 (refer to Figure 8.1), which is situated at the crack site on the playground of Nishi

Araya Elementary School. These profiles represent the results obtained from the SDS test, PDC test, and PDCPT.

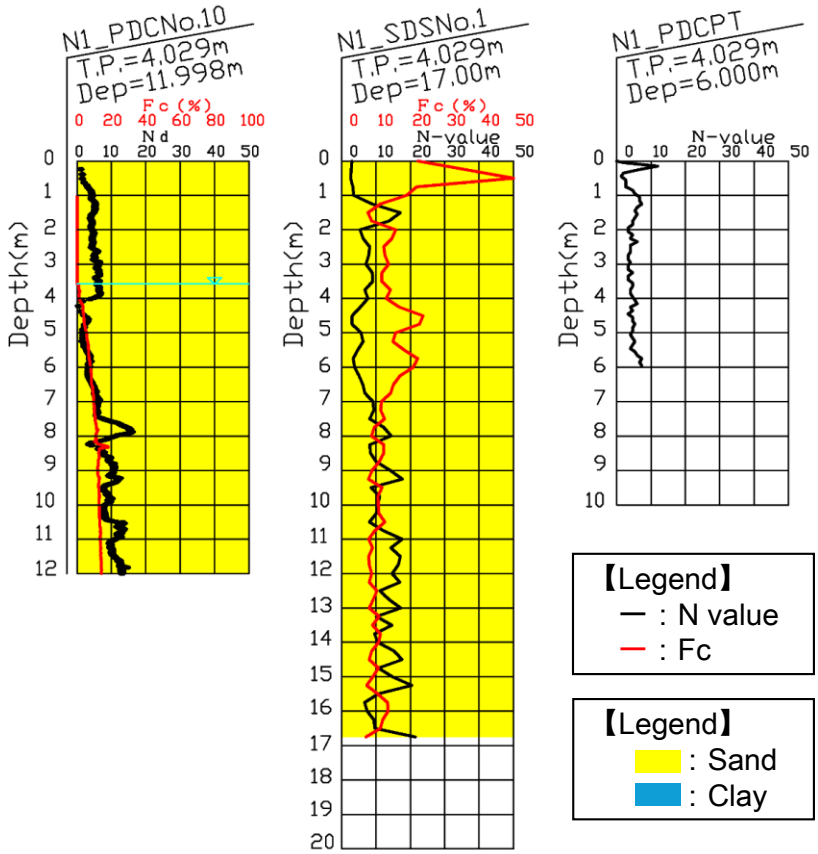

Figure 8.9. Comparison among the SDS test, PDC test, and PDCPT results at location N1 in the elementary school's playground

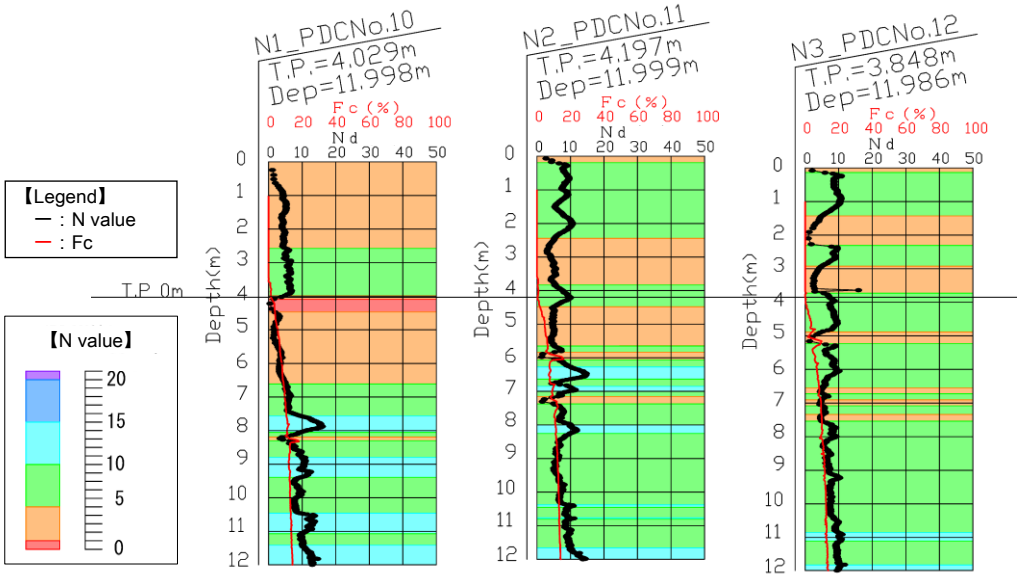

Figure 8.10. PDC results at locations N1, N2 and N3 in the elementary school's playground

As observed from Fig. 8.9, for all tests, N-values remain below 10 up to a depth of 6 to 7 meters, indicating that the soil remains in a loose state following the earthquake. A gradual

increase in N-values with depth is observed beyond this point, as indicated by the PDC and SDS test results. It should be noted that PDCPT tests were conducted only to depths of 5 to 7 meters, depending on the specific location. Additionally, based on the fine content (Fc) estimates from the PDC and SDS tests, it is inferred that sandy soil with Fc < 50% extends to a depth of approximately 17 meters below the surface. The discrepancy in the estimated fine content (Fc) between the PDC and SDS tests is attributed to the differing methodologies: the PDC test estimates fine content based solely on pore water pressure, whereas the SDS test uses two parameters—torque and applied load. As a result, when torque values show little variation, the estimated Fc is likely to be more influenced by the applied load.

Figure 8.10 presents the profiles of N-values and fine content with depth from the PDC tests conducted at locations N1, N2, and N3. The results reveal a loose soil zone with N-values below 5 extending to a depth of approximately 6 meters. Notably, a very loose soil layer, characterized by N-values ranging from 0 to 1, is localized around 4 meters in depth at location N1, situated toward the Uchinada sand dunes, as indicated by the penetration data.

8.3 Case Study 2: Field Survey and Results for the Muro Area

Figure 8.11 illustrates the locations of the field surveys conducted in the Muro area. The figure highlights the positions of the PDC tests, SDS tests, and PDCPT, represented by yellow circles, squares, diamonds, triangles, and inverted triangles, respectively.

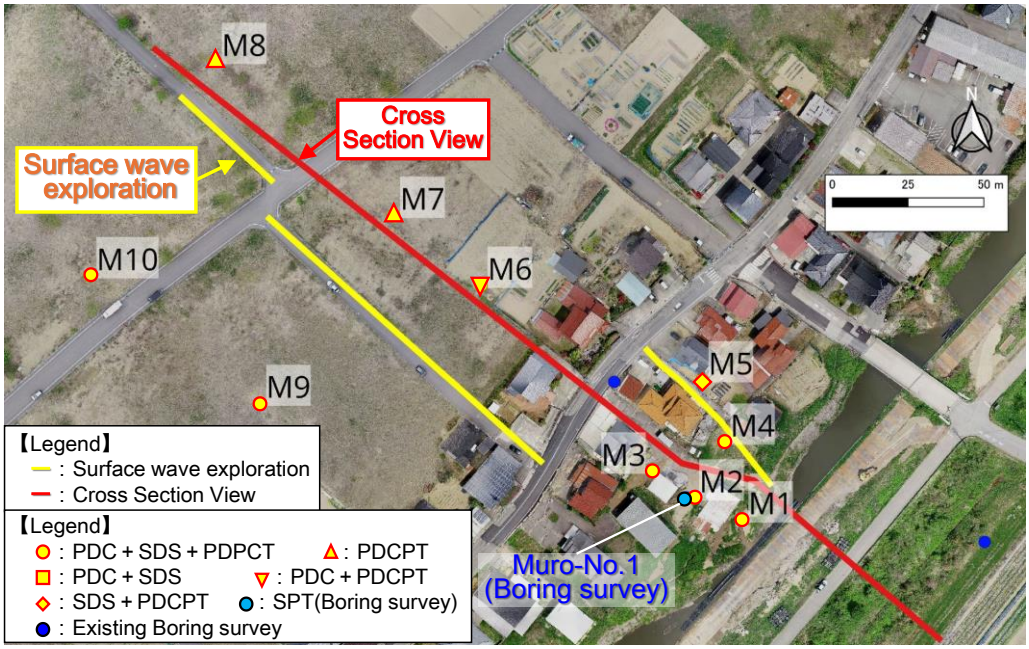

Figure 8.11. Field survey locations in the Muro area

The light blue circle (Muro No. 1) indicates the location of SPT performed by the authors, while the dark blue circle marks the position of an existing boring survey. The yellow lines represent the areas where surface wave exploration tests were conducted. Additionally, 3D laser scanning was carried out in this region. These locations were selected to assess the

geotechnical and geological characteristics of the Muro area, where a house was displaced by 12 meters due to liquefaction-induced lateral spreading (refer to Figure 5.31). In contrast, a nearby pile-supported house (① in Figure 5.31) was not affected by lateral flow.

8.3.1 3D Laser Scanning

Figure 8.12 presents a comparison between pre-disaster aerial photographs and post-disaster point cloud data obtained through 3D laser scanning.

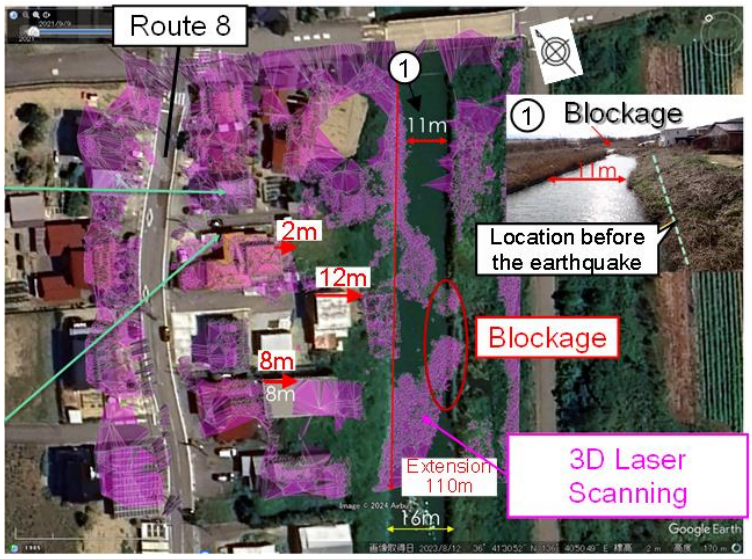

Figure 8.12. Comparison of 3D laser scanner survey results (after the disaster) and aerial photographs (before the disaster) in the Muro area

The figure clearly shows that houses on the eastern side of Prefectural Road No. 8, facing the waterway, had shifted by approximately 2 to 12 meters toward the waterway. Furthermore, the surrounding ground of these houses also displaced toward the waterway, causing a shift in the waterway itself over a distance of about 11 meters, with some areas nearly obstructing the majority of the waterway. In contrast, no significant movement was observed in the houses situated on the mountainside (Uchinada sand dunes side), including those along Prefectural Road No. 8.

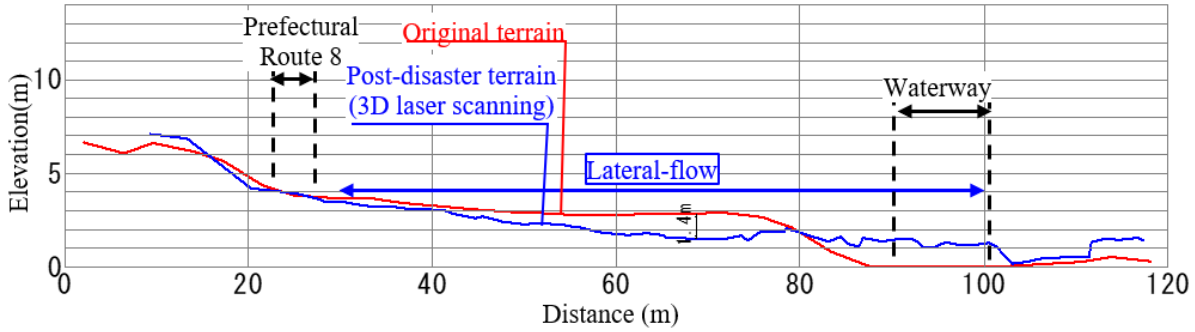

Figure 8.13. Comparison between existing topographic data (GSI) and 3D laser scanner survey results

At the location exhibiting the greatest lateral displacement, a comparison was made between the pre-disaster topography (represented by the red line, based on 5m mesh DEM data from October 5, 2016) and the post-disaster topography (represented by the blue line, based on remote sensing data from February 4, 2024), as shown in Figure 8.13. The comparison revealed that the maximum lateral displacement of the ground caused by liquefaction-induced lateral spreading was approximately 20 meters, which resulted in the blockage of most of the waterway. Furthermore, the ground surface experienced a maximum settlement of about 1.4 meters. In contrast, minimal to no changes in ground elevation were observed on the western side of Prefectural Road 8.

8.3.2 Portable Dynamic Cone Penetration Test (PDCPT) Tests

The authors have collected the pre-construction N-value data from the owner of the pile supported house. Additionally, since the soils surrounding the foundation had flowed and subsided due to liquefaction, PDCPT testing could be conducted from the depth of 1.7 meters below the foundation (location a in Fig. 8.14). Further PDCPT tests were also carried out in the free field, 5 meters away from the house (location b), as shown in Figure 8.14. By analyzing the N-value data and observing the changes before and after the Noto Earthquake, we can gain valuable insights into the causes of the soil failure near the foundation.

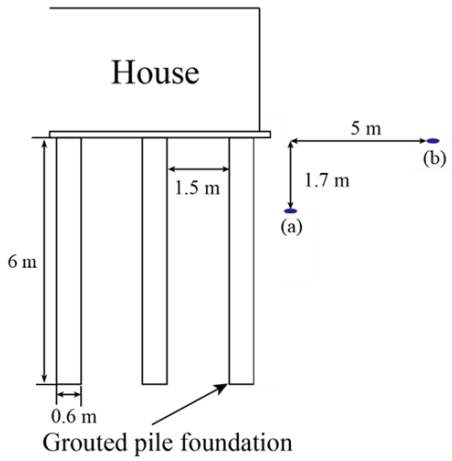

Figure 8.14. Location of PDCPT (a) and (b)

Figure 8.15 reveals that, prior to the foundation installation, the N-values at depths of approximately 1.5 m and 3 m were around 10, indicating adequate bearing capacity. However, post-earthquake N-value data show that, between depths of 2.2 m and 4.2 m, the N-values were consistently below 2, suggesting very soft soil within this section. Below 4.2 m, two N-value readings are relatively similar. A comparison with data from the same location (Fig. 8.15a) indicates that the 2.5-meter depth range, from 1.7 m to 4.2 m, was significantly impacted by the earthquake. The water table was observed at 4.1 m below the foundation. Additionally, the N-values in Figure 8.15(b) suggest that the soil remained highly susceptible to liquefaction following the earthquake. Figure 8.16 illustrates the locations of the PDCPT tests conducted across the Muro area, while Figure 8.17 presents the converted N-values along the depth at various locations.

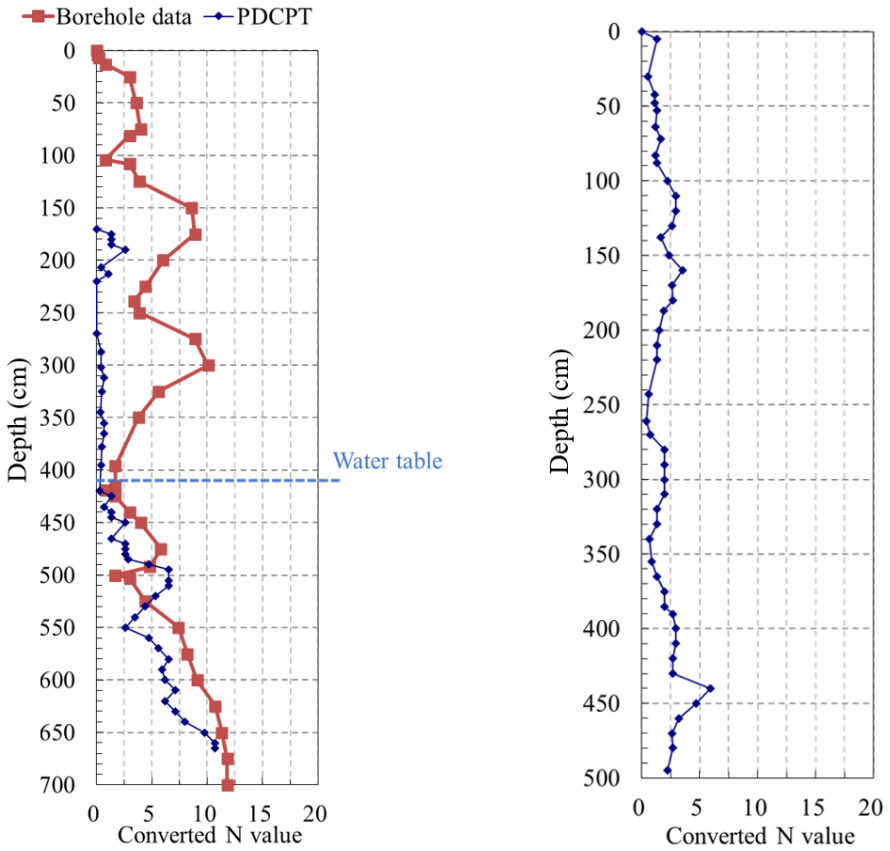

Figure 8.15. Converted N-values along the penetration depth at locations (a) and (b)

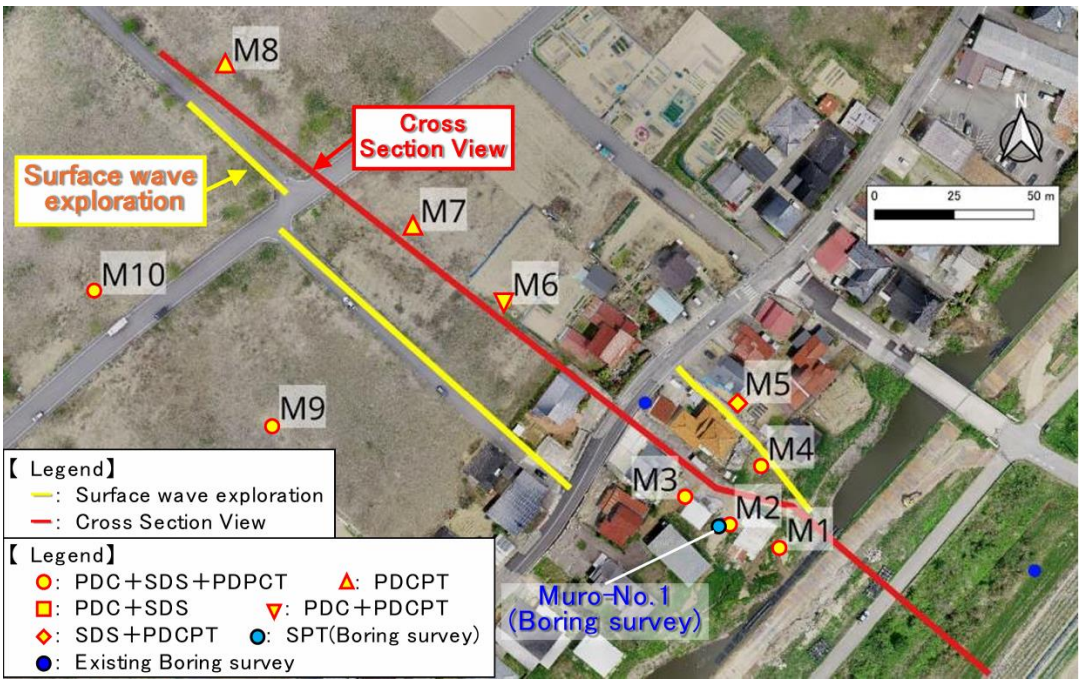

Figure 8.16. Location of PDCPT in Muro area

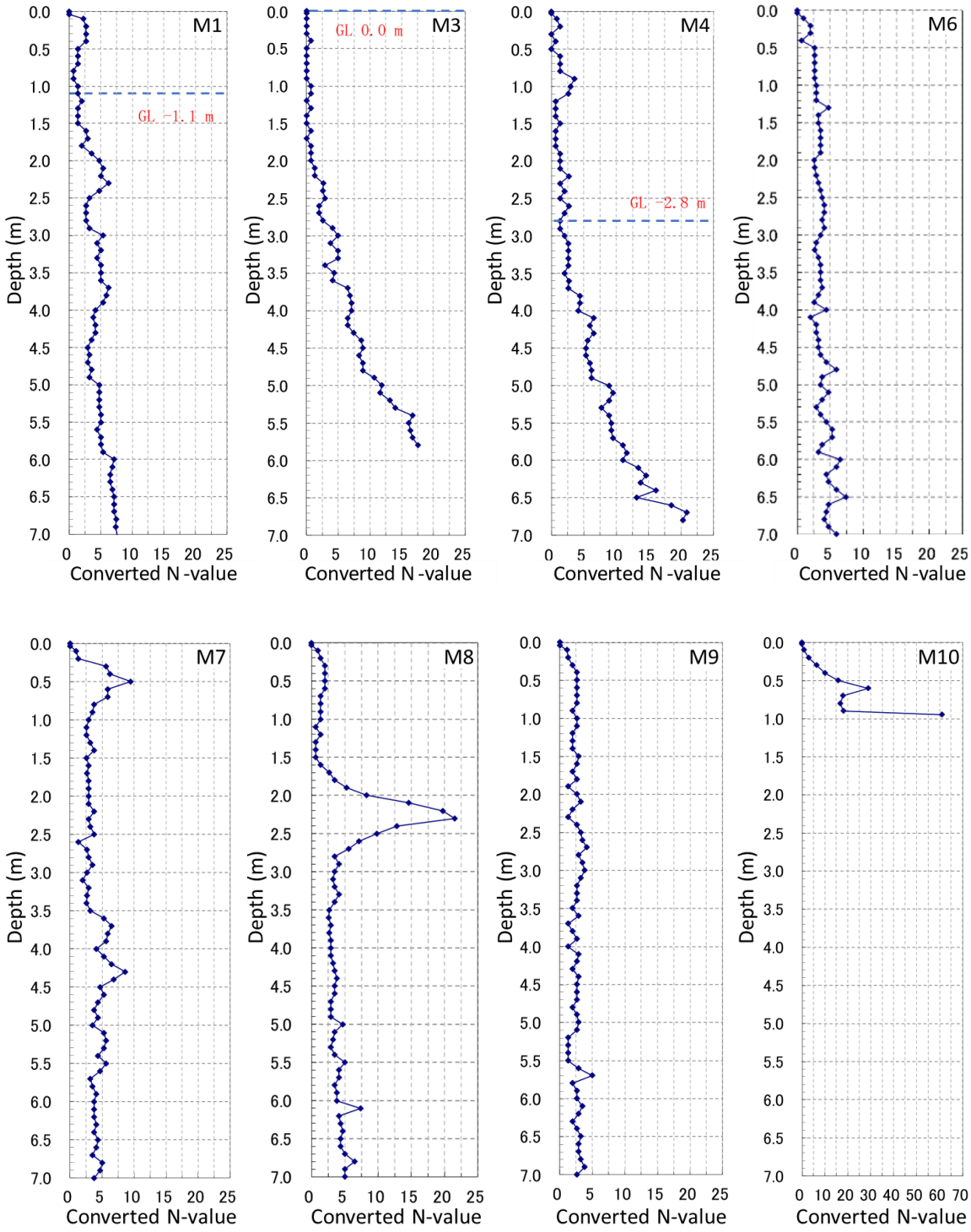

Figure 8.17. Converted N-value along the penetration depth

M1, M3, and M4: These locations show varying groundwater levels (GL-1.1 m, GL-0 m, and GL-2.8 m, respectively), which directly impact the soil's vulnerability to liquefaction. The lower N-values and fluctuating profiles at M1 and M3 suggest that these sites may have experienced notable softening and density reduction due to the earthquake. M3, with groundwater at the surface, likely saw extensive liquefaction, contributing to its decreased resistance and heightened susceptibility to lateral spreading. The post-liquefaction N-values at

M4, showing a denser layer at GL-2.8 m, may indicate partial resilience or recovery of this layer, while the looser upper layers remain vulnerable.

M6, M7, M8, and M9: These locations, without observed groundwater levels, show moderate to uniform N-values, indicating that while they may have been affected by seismic shaking, they did not experience the same level of liquefaction as fully saturated sites. M8's denser layer at shallow depth may suggest partial resilience to the liquefaction process, while M6, M7, and M9 show relatively consistent profiles, which could indicate a more stable response to the earthquake-induced liquefaction.

M10: The limited penetration depth at M10 (approximately 1 m) highlights a dense subsurface layer that withstood liquefaction and lateral movement, suggesting strong resistance to deformation. The dense material beneath the upper layer may have acted as a natural barrier, preventing deeper liquefaction effects in this area. This density provides an interesting contrast to other locations, suggesting that pre-existing dense layers may reduce post-liquefaction vulnerability and lateral spreading, which is crucial information for future mitigation planning.

The PDCPT results indicate that sites with shallow or surface-level groundwater (e.g., M3) experienced severe liquefaction and subsequent loss of resistance, leading to significant ground deformation and lateral movement. In contrast, sites with dense underlying layers (such as M10) demonstrated resilience to liquefaction, suggesting that pre-existing density and stratification play a critical role in post-earthquake stability. This understanding can inform future ground improvement efforts, targeting loose or fully saturated zones and incorporating strategies to strengthen or densify susceptible layers to mitigate liquefaction risk in similar seismic environments.

8.3.3 Screw Driver Sounding (SDS) Tests

Figure 8.18 illustrates the relationship between the corrected torque and elevation, while Figure 8.19 depicts the relationship between the converted N-value and depth at survey points M1 through M3. The results from the SDS test indicate that the corrected torque values within the 2-4 m depth range were quite low, with a response similar to that of cohesive soils. However, it is likely that liquefaction of the underlying sandy soil led to a significant reduction in the stiffness of the overlying cohesive soil layer. A thin clay layer was observed at an elevation of -2 m at survey points M1 and M2. Relatively higher N-values were recorded at the -5 m elevation at M2 and M3, and soil below -4 m was identified as clayey based on the test results. The estimated N-value from the SDS testing was lower than that obtained via the SPT at an elevation of +3 m at M2; however, a good agreement was observed under higher confining stress. Based on the test data, it can be concluded that liquefaction likely occurred in the shallow depth range between 2 m and 4 m, as both the corrected torque and converted N-values were notably low in this zone.

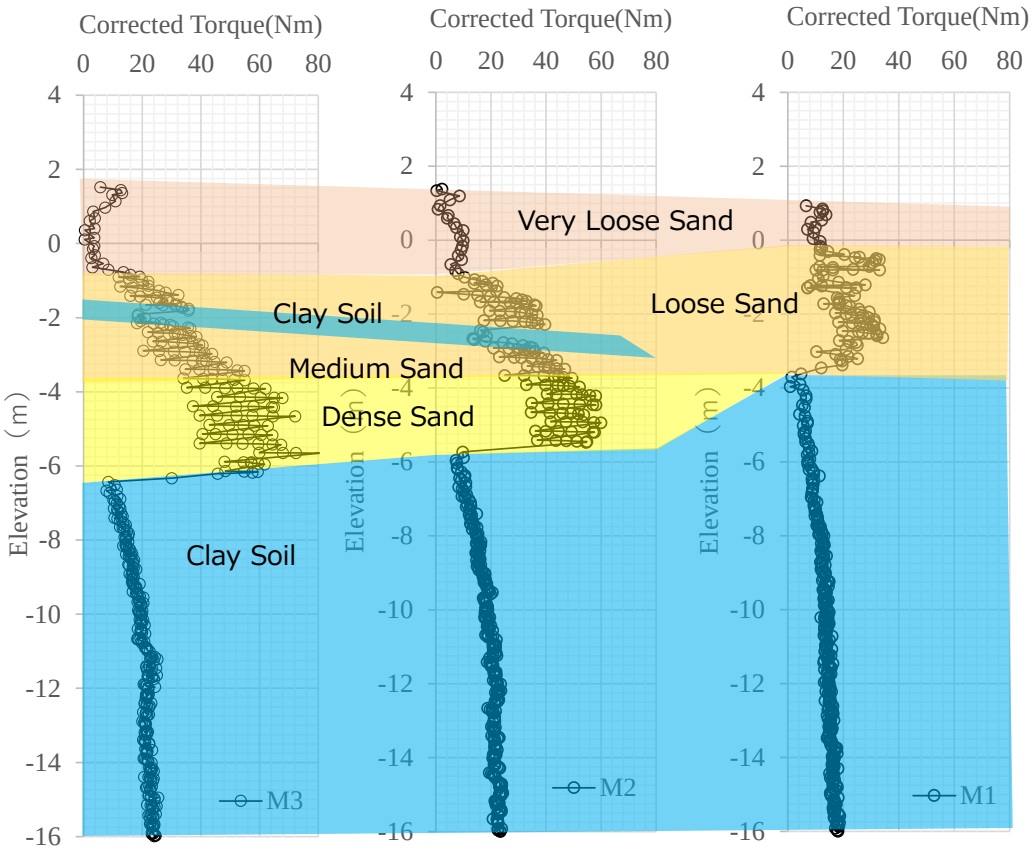

Figure 8.18. Relationship between corrected torque and elevation

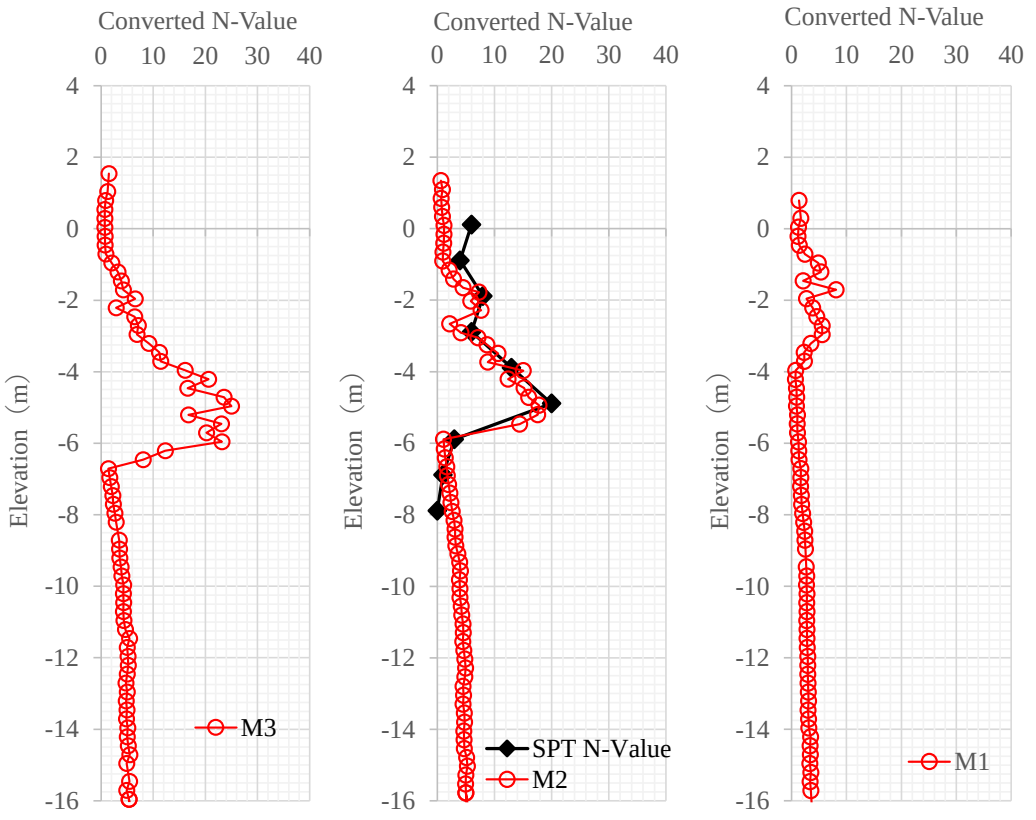

Figure 8.19. Relationship between converted N-value and elevation

8.3.4 Piezo Drive Cone (PDC) Tests

Similar to the Nishi Araya area, the PDC test was used to classify the soil types in this area. The results indicated that both the buried soil layer (Fs) and the dune layer (Sd1) on the reclaimed land side were predominantly sandy layers with negligible fine-grain content, as illustrated in Figure 8.20.

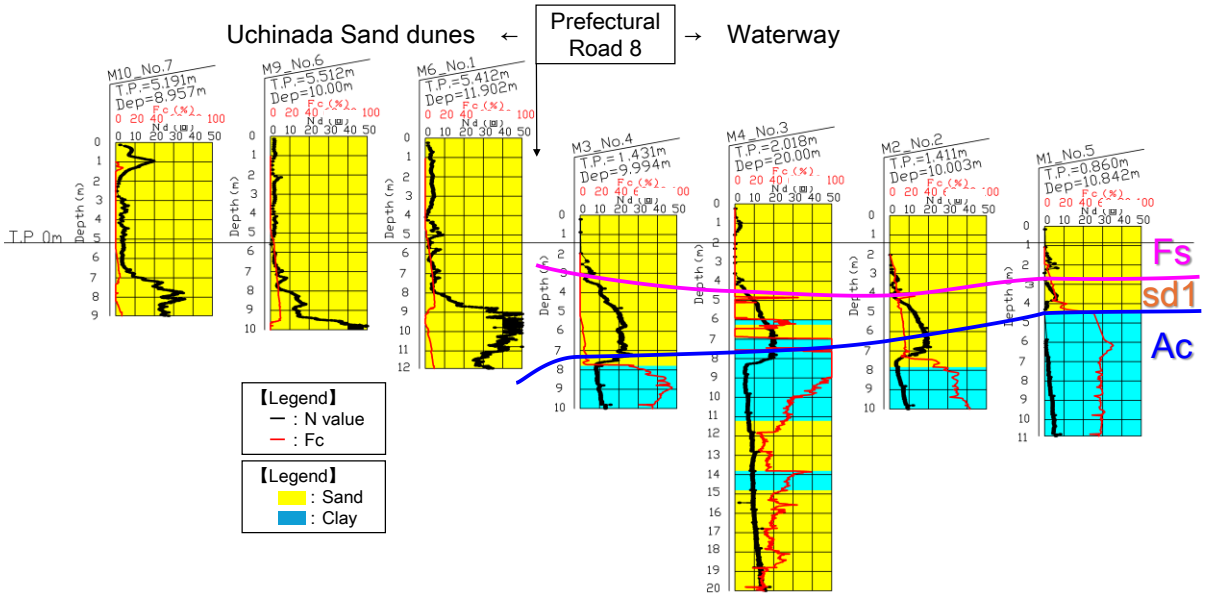

Figure 8.20. Depth profiles of fine grain content Fc based on PDC test (Muro area).

8.3.5 Surface Wave Exploration Tests

The cross-sectional diagram of the S-wave velocity (Vs) obtained from surface wave exploration is shown in Figure 8.21.

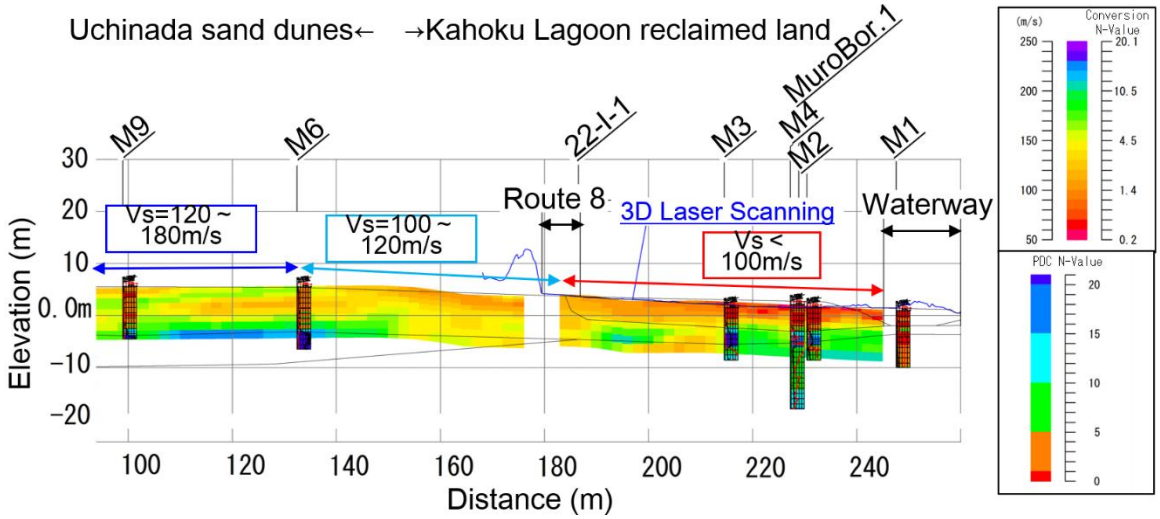

Figure 8.21. Result of surface wave exploration survey in the Muro area

The distribution of S-wave velocities reveals that the region on the mountainside (sand dunes side) of Prefectural Road 8 exhibits S-wave velocities ranging from 100 to 180 m/s, while the area on the waterway side of the road shows a significant reduction, with S-wave velocities of

less than 100 m/s. This lower velocity zone roughly corresponds to the fill layer (Fs) and the very loose area (with N-values between 0 and 1) identified in the PDC test. The relatively low S-wave velocity within the fill layer, composed primarily of dune sand, is attributed to the land reclamation efforts conducted in the 1930s, suggesting that the fill was not adequately compacted.

Focusing on variations within the fill layer, it is noteworthy that localized zones with particularly low S-wave velocities are present near the waterway. These areas are associated with liquefaction-induced sand boils and lateral flow, which caused blockages in the waterway. It is likely that lateral flow due to liquefaction has contributed to soil looseness and a reduction in shear stiffness in this region. The boundary between the fill layer and the natural sand dune layer (Fs) is assumed to be located near Prefectural Road 8. However, the S-wave velocity distribution indicates an additional zone with S-wave velocities ranging from 100 to 120 m/s, extending approximately 40 meters from the edge of the fill layer. This area displays features such as tensile cracks and step-like terrain, which are indicative of flow slides. These characteristics suggest that secondary slope movements may have occurred due to lateral flow within the fill layer.

8.3.6 Comparison of Sounding Test Results

Figure 8.22 illustrates the depth profiles of equivalent N-values and fine content (Fc) at location M2, where sand boils were observed, representing the test results from the SDS test, PDC test, and PDCPT. All tests indicate equivalent N-values between 0 and 1 at a depth of approximately 2 meters, signifying an extremely loose soil condition. The higher N-values obtained from the SPT at around 2 meters, compared to the equivalent N-values from the SDS and PDC tests, are likely due to the SPT being conducted four months after the other tests, suggesting that the ground stiffness may have recovered during that period. Below 2 meters, the equivalent N-values gradually increase to approximately 20 by 6 meters, after which a decrease in equivalent N-values and an increase in fine content (Fc) are observed around 8 meters.

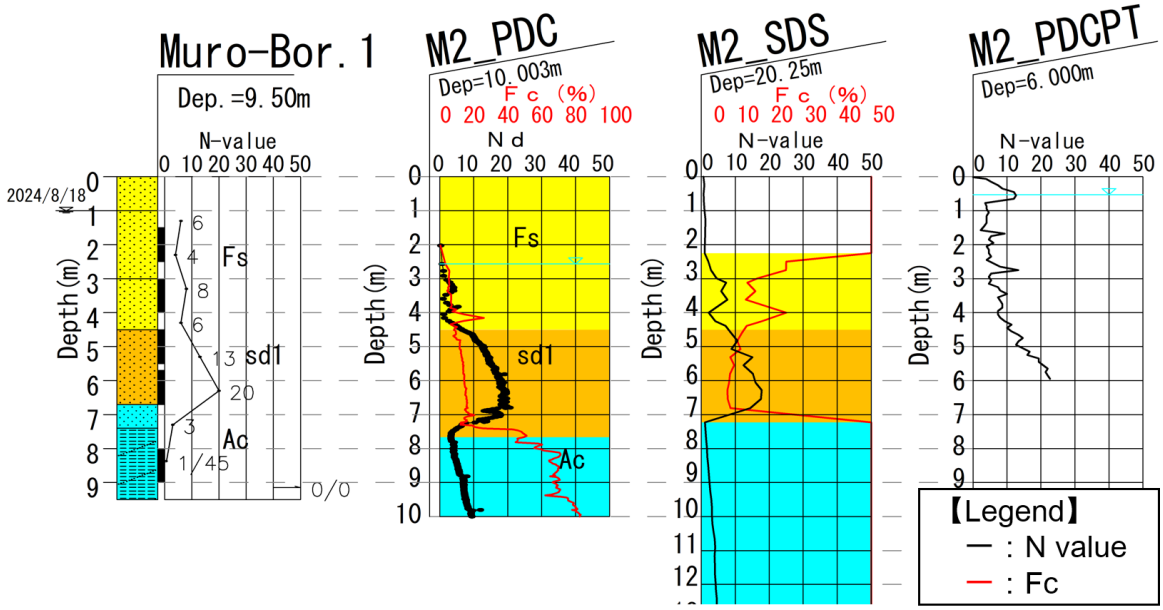

Figure 8.22. Comparison of N value and fine content, Fc at a representative location (M2)

Based on the comparison outlined above, the N-values were zoned using the depth profiles of N-values and fine content (Fc) obtained from the PDC test along the cross-section, as shown in Figure 8.23. For soil classification, areas with low N-values and fine content (Fc) exceeding 50% were categorized as clayey soil. The results of this classification are presented in the geological cross-section in Figure 8.24.

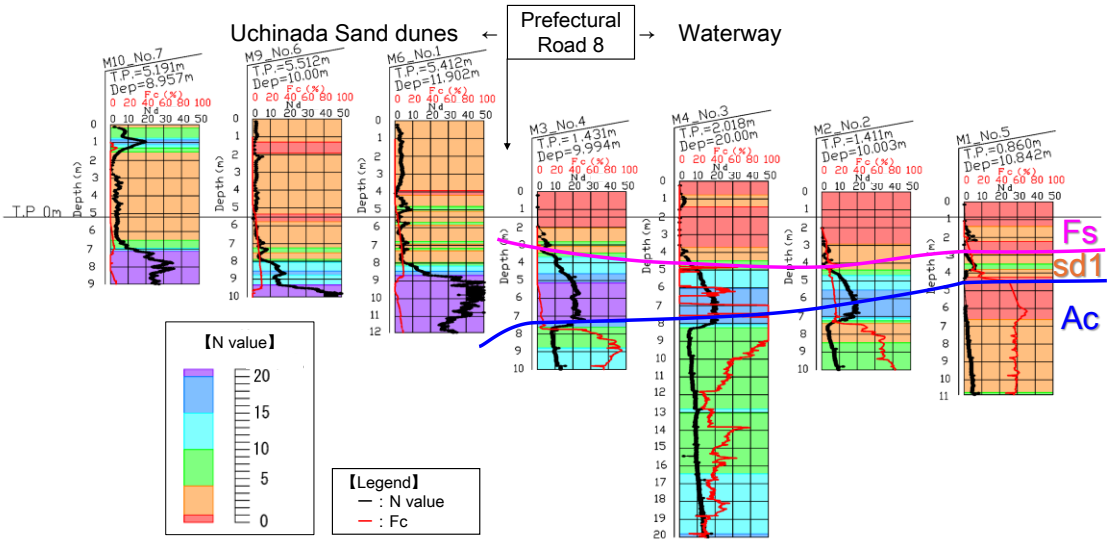

Figure 8.23. PDC test results in the cross section

As previously mentioned, the Muro area is reclaimed land, created by filling the edge of the sand dunes facing Kahoku Lagoon with sandy soil. Very loose zones, with N-values ranging from 0 to 1, are observed continuously at depths of approximately 2 to 4 meters on the waterway side (east side) of Prefectural Road 8, where the fill layer is present. In contrast, on the mountainside (west side) of the road, where the sand dunes are located, although localized areas with N-values of 0 to 1 are present, this trend is not observed to be continuous.

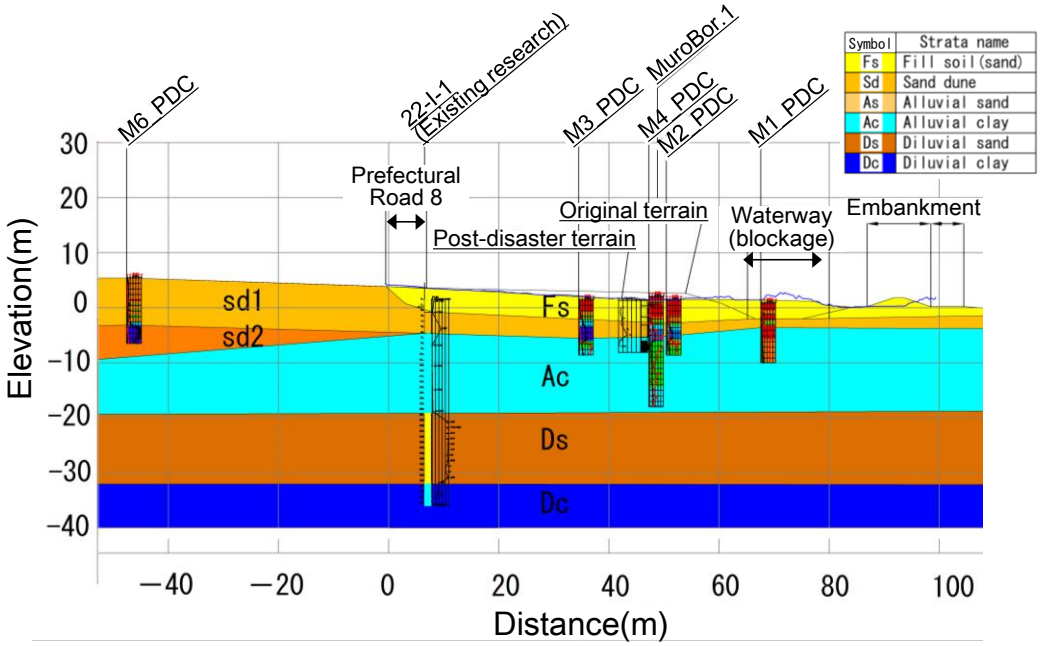

Figure 8.24. Estimated geologic cross section obtained from PDC test

9. Discussion on the Results

In the liquefaction-affected areas of Uchinada Town, particularly Nishi Araya and Muro, where significant lateral movement was observed, various field tests—including the PDC test, SDS test, PDCPT, and surface wave exploration—were conducted to evaluate ground hardness and soil classification. The following observations were made based on the test results:

1) Loose Soil Layers in Nishi Araya: In the Nishi Araya area, loose zones with N-values below 5 were observed up to a depth of approximately 6 meters. Additionally, a highly loose zone with N-values between 0 and 1 was localized at a depth of around 4 meters on the Uchinada sand dune side.
2) Soil Classification from PDC Test: Zoning of N-values was performed using the depth profiles of N-values and fine content (Fc) obtained from the PDC test. Soils with low N-values and fine content exceeding 50% were classified as clayey soil and were delineated accordingly in the cross-sectional diagrams.
3) Very Loose Zones in Muro: In the Muro area, a continuous zone of very loose soil with N-values between 0 and 1 was identified on the waterway side of Prefectural Road No. 8, extending to depths of approximately 2 to 4 meters. In contrast, on the mountainside of the road, while localized zones with N-values of 0 to 1 were present, no significant continuity was observed.
4) SDS Test Results: N-values estimated from the SDS test were lower than those measured using the SPT in zones of lower confining stress, but good agreement was observed under higher confining stress conditions. The SDS test results suggest that liquefaction likely occurred at relatively shallow depths (2 to 4 meters), as indicated by small, corrected torque and converted N-values within this range.
5) Surface Wave Exploration: Surface wave exploration revealed S-wave velocities of 100 to 180 m/s on the mountainside (west side) of Prefectural Road No. 8, while the waterway side exhibited lower velocities (less than 100 m/s). These low-velocity zones corresponded to the fill layer consisting of very loose sand (N-values of 0 to 1), as confirmed by the PDC test.
6) Shallow Liquefaction in Muro Area: The combined results of the ground investigations suggest that liquefaction likely occurred at very shallow depths (approximately 1 to 3 meters from the ground surface) in the Muro area, leading to extensive damage observed in the region.

10. Factorial analysis on lateral flow induced damage and lessons learned

Based on field investigations and stakeholder interviews, the authors have identified five potential factors contributing to the widespread liquefaction observed in the area located approximately 100 kilometers from the earthquake epicenter.

a. Amplification of motion: Figure 10.1 presents the existing boring survey data from the Muro area. The data reveal the presence of a 15-meter-thick layer of very soft clay, which may have amplified seismic motion, thereby contributing to the extensive and localized liquefaction observed across the area.

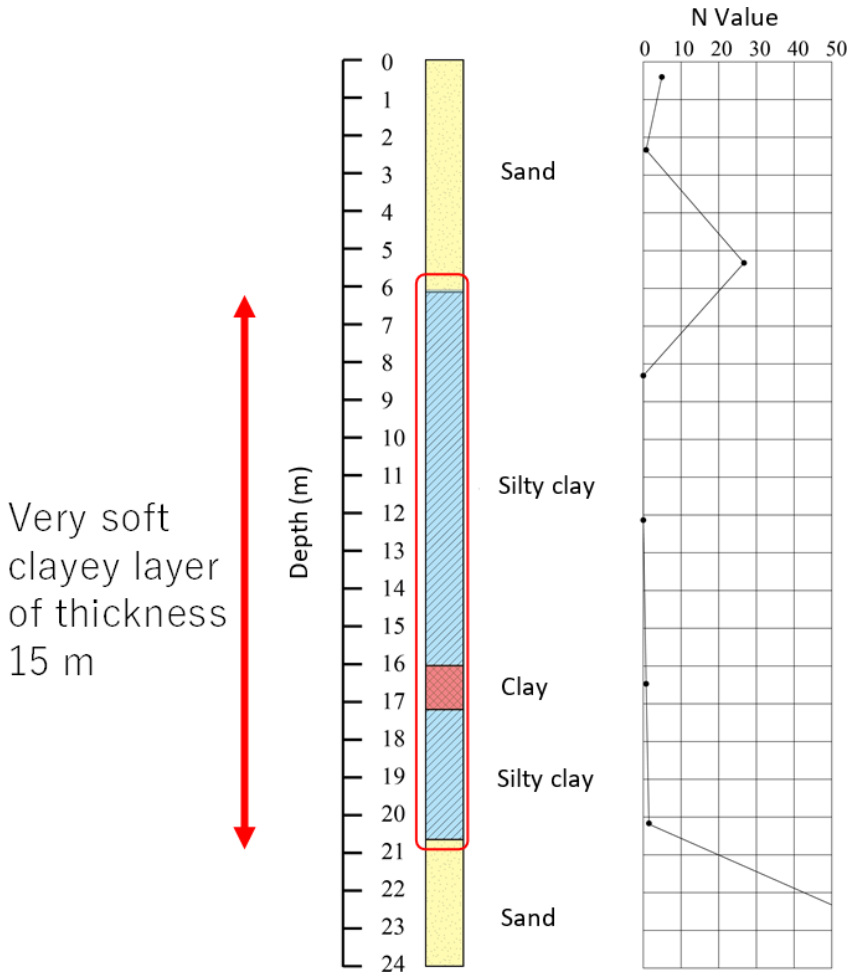

Figure 10.1. Existing boring survey data

b. Short predominant period with high velocity: Figure 10.2 illustrates the acceleration record from the station nearest to Uchinada Town, along with the corresponding response velocity spectra. The velocity spectrum exhibits a pronounced dominance of short periods, with a notably high response velocity of 60 cm/s. This indicates that the substantial seismic energy generated during the event may have been another contributing factor to the widespread and localized liquefaction observed in the area.

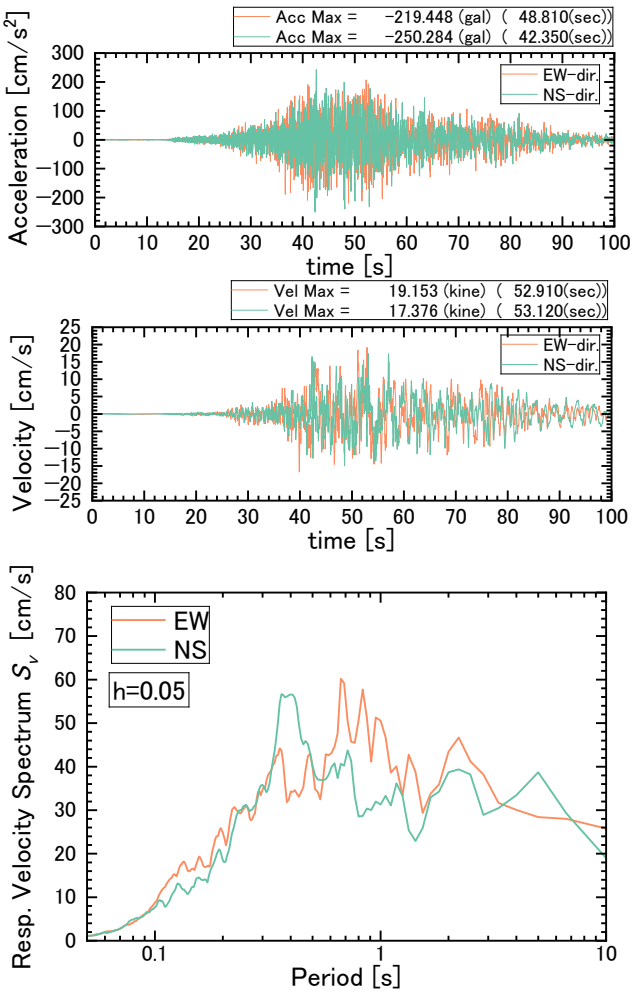

Figure 10.2. Acceleration record and response spectra

c. Landfilling and high-water table: Both the Nishi Araya and Muro areas of Uchinada Town are reclaimed land with a high-water table. During the post-disaster survey, significant water accumulation was observed along the periphery of the reclaimed land in the Muro area (Fig. 10.3). Additionally, a contour map generated using pre-disaster elevation data (Fig. 10.4) revealed that the areas affected by lateral movement displayed concave terrain typical of a drainage basin, indicating a high groundwater level.

Figure 10.3. Waters seen during the post disaster survey

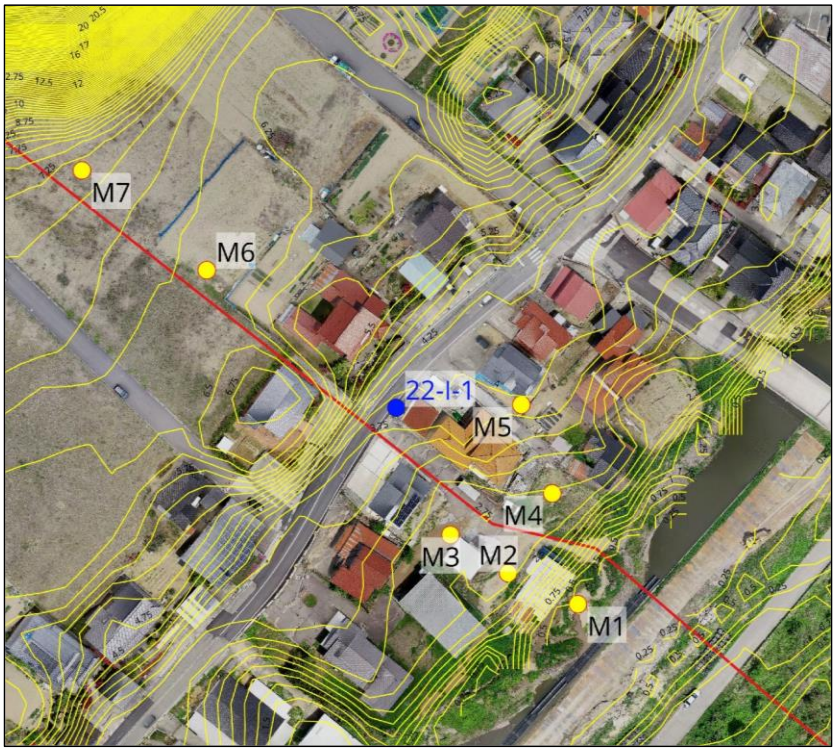

Figure 10.4. Contour map using the pre-disaster elevation data

d. Liquefaction at shallow depth: Our post-disaster boring investigation revealed that the water table in the Muro area was located within 1.0 meter of the ground surface. The upper 4.5 meters of the soil consisted of fill material with N-values less than 5, underlain by an original sand dune layer approximately 2.2 meters thick, with N-values ranging from 15 to 20. Based on this data, it can be inferred that liquefaction likely occurred at a relatively shallow depth, between 1.5 and 2.0 meters below the ground surface. This inference is further supported by observations of manhole behavior in Uchinada Town. Figure 10.5 illustrates the post-disaster condition of manholes in Uchinada Town and Suzu City. While no manhole uplift was observed in Uchinada Town, significant uplift exceeding 1.6 meters was recorded in Suzu City.

(a) Suzu city (b) Uchinada town

Figure 10.5. Manhole upliftment

e. Suppression of Lateral Flow by Prefectural Road No. 8: Figure 10.6 depicts the condition of Prefectural Road No. 8 near the Nishi Araya area. Our survey revealed that most of the lateral flow was effectively halted on the west side of the road. This obstruction resulted in substantial compressive forces acting on the road, leading to ground uplift on its western side. The observed compression and uplift are presumed to have been influenced by the compaction of the road surface caused by repeated traffic-induced vibrations over many years. Consequently, the road acted as a structural barrier, effectively suppressing significant lateral flow in the area.

Figure 10.6. Compression and upliftment of prefectural road no. 8 (Near Nishi Araya area)

11. Conclusions and future directions of research

Based on the two case studies conducted, the following conclusions can be drawn:

1) Ground Conditions Favorable for Liquefaction: Boring survey results indicate that the fill material in the study area predominantly consists of fine sand. Additionally, the cutting of sand dunes during land reclamation elevated the groundwater table, creating conditions conducive to liquefaction.
2) Shallow Liquefaction Depth: Ground investigations suggest that liquefaction likely occurred at shallow depths, approximately 1 to 2 meters below the surface.
3) Extremely Loose Soil on the East Side of Prefectural Road No. 8: Surface wave exploration revealed that the east side of Prefectural Road No. 8 exhibited extremely low S-wave velocities (less than 100 m/s), corresponding to a very loose fill layer consisting of sand with N-values ranging from 0 to 1, as corroborated by PDC test results.
4) Low Strength Indicators in SDS Test Results: SDS test results showed that the corrected torque and converted N-values were significantly low within depths of 2 to 4 meters, further supporting the hypothesis that liquefaction occurred at these shallow depths.
5) Amplification Through Alluvial Clay: Both the existing boring data and the geological cross-section from PDC testing identified a 15-meter-thick alluvial clay layer located approximately 6 meters below the surface. Amplification of seismic waves through this clay layer is believed to have been a significant factor contributing to the widespread liquefaction observed.
6) Lateral Spreading in the Muro Area: In the gently sloping terrain of the Muro area, liquefaction likely occurred at shallow depths (within 1 to 2 meters), resulting in significant lateral spreading and associated damage. The absence of pronounced manhole uplift in Uchinada Town further supports the conclusion that liquefaction primarily occurred at shallow depths.
7) Performance of Pile-Supported Foundations: For structures with foundations supported by improved piles, voids were observed beneath the foundations due to liquefaction. However, no evidence of differential settlement or lateral displacement of the structures was recorded.
8) Prefectural Road No. 8 as a Barrier: Prefectural Road No. 8 acted as an effective barrier against lateral spreading, leading to ground uplift along its western side. This suppression of lateral spreading is attributed to the compaction and hardening of the ground beneath the pavement over time, likely caused by repeated traffic-induced loading.

To mitigate liquefaction-induced damage in the region during future earthquakes, the following key challenges must be addressed:

- Comprehensive Investigation of Groundwater Levels: Conduct detailed and systematic investigations of groundwater levels to better understand their role in triggering liquefaction.
- Enhancement of Liquefaction Hazard Maps: Refine existing liquefaction hazard maps by incorporating extensive and high-resolution ground data to improve their accuracy and reliability.

- Inclusion of Lateral Flow Risks in Hazard Maps: Develop new liquefaction hazard maps that explicitly account for the risk of lateral flow, providing a more holistic assessment of potential hazards.
- Evaluation of Groundwater-Lowering Techniques: Explore and assess groundwater-lowering methods based on thorough ground surveys to minimize the risk of unintended settlements caused by underlying clay layers saturated with water.
- Cost-Effective Ground Improvement for Residential Areas: Implement economical and efficient ground improvement techniques to enhance the resilience of residential buildings located in high-risk areas.

References

Cabinet Office of Japan (2014). “Damage from the 2024 Noto Peninsula Earthquake, 2024.” https://www.bousai.go.jp/updates/r60101notojishin/r60101notojishin/pdf/r60101notojishin_49.pdf

Fire and Disaster Management Agency (2024). “Damage caused by the 2024 Noto Peninsula Earthquake and Response status of fire departments, etc.” (109th report)] Retrieved 16 October 2024. [in Japanese]

Fuji, N. (1971). “Chronology and paleoenvironmental condition for the formation of the buried humus soils of the coastal sand dunes area in the Hokuriku District, Central Japan.” The Quaternary Research, *Journal of Japan Association for Quaternary Research*, 10(3), 134-146 [in Japanese].

Fujishiro, T., Hazarika, H., Matsumoto, T., and Ishizawa, T. (2024). “Overview of liquefaction damage in Kahoku City and Uchinada Town due to the 2024 Noto Peninsula Earthquake- (Part 1).” *In: 59th Annual Conference of Japanese Geotechnical Society, Asahikawa, Japan*, paper ID: [23-12-2-06]. [in Japanese]

Geospatial Information Authority of Japan (2024). “Landslide and sediment distribution data and map for the 2024 Noto Peninsula Earthquake.” https://www.gsi.go.jp/BOUSAI/20240101_noto_earthquake.html (Accessed: August 8, 2024). [in Japanese]

Hayashi, K., Suzuki, H., and Saito, H. (2001). “Surface wave method using artificial sources development and application to civil engineering investigations.” *OYO technical report 2001*, pp. 9-39, https://www.oyo.co.jp/pdf/technology_annual/2001_03.pdf.

Hazarika, H., Ohta, S., Kubota, S., Michi, Y., Sahare, A., Tanaka, T., Ishizawa, T., Murai, M., Fujishiro, T., Matsumoto, T., and Hyodo, T. (2024). “Lateral Flow in Reclaimed Land due to Liquefaction during the 2024 Noto Peninsula Earthquake, Japan ~ Insights from Remote Sensing and Field Survey ~” *In: 8th International Conference on Recent Advances in Geotechnical Earthquake Engineering and Soil Dynamics, IIT Guwahati, India*.

Hazarika, H., Ishizawa, T., Matsumoto, T., Murai, M., Fujishiro, T., Ohta, S., and Michi, Y. (2024). “Analysis of liquefaction damage in Uchinada Town due to the 2024 Noto Peninsula earthquake.” *In: 59th Annual Conference of Japanese Geotechnical Society, Asahikawa, Japan*, paper ID: [25-13-1-04]. [in Japanese]

Hu, Y., Qin, C., Hazarika, H., Sahare, A., Kubota, S., and Harima, Y. (2024). “Liquefaction damage in the Muro district of Uchinada Town due to the 2024 Noto Peninsula earthquake- (Part 2).” *In: 59th Annual Conference of Japanese Geotechnical Society, Asahikawa, Japan*, paper ID: [25-13-1-02].

Ishii, K., Totake, N., Yoshimura, T., Iwagami, J., Kuriyama, H. and Yabe, M. (2024). “Estimation Methodology for Estimating the Impact of the 2024 Noto Peninsula Earthquake, Economic and Fiscal Analysis Discussion Paper DP/24-1.” *Cabinet Office of Japan*, 44p, 2024.

Inoue, T., and Okamura, Y. (2010). “Explanatory notes of 1:200,000 marine geological map around the northern part of Noto Peninsula.” 14p, 2010

Japan Meteorological Agency (2024). https://web.archive.org/web/20240101081217/https://www.data.jma.go.jp/multi/quake/quake_detail.html?eventID=20240101161648&lang=en. Retrieved 16 October 2024.

Kubota, S., Ohta, S., Ochi, Y., Michi, Y., Fujishiro, T., Hazarika, H., Murai, M., and Tanaka, T. (2024a). “Liquefaction damage in the Muro district of Uchinada Town due to the 2024 Noto Peninsula earthquake- (Part 3).” *In: 59th Annual Conference of Japanese Geotechnical Society, Asahikawa, Japan*, paper ID: [25-13-1-03]. [in Japanese]

Kubota, S., Ohta, S., Hazarika, H., Matsumoto, T., Tanaka, T., Murai, M., Fujishiro, T., and Michi, Y. (2024b). “Investigation report aiming to elucidate the mechanism of liquefaction damage in the Muro district of Uchinada Town due to the 2024 Noto Peninsula Earthquake (Part 1).” *Journal of Japan Society for Natural Disaster* (to appear in December 2024). [in Japanese]

Kubota, S., Ohta, S., Ochi, Y., Imai, T., Hazarika, H., Matsumoto, T., Tanaka, T., Murai, M. (2024c). “Investigation report aiming to elucidate the mechanism of liquefaction damage in the Muro district of Uchinada Town due to the 2024 Noto Peninsula Earthquake (Part 2).” *Journal of Japan Society for Natural Disaster* (to appear in December 2024). [in Japanese]

Machida, H., Matsuda, T., Umitsu, M., Koizumi, T. (2006). “Chubu Topography of Japan.” *The University of Tokyo Press*, Tokyo, 392p, 2006

Michi, Y., Fujishiro, T., Matsumoto, T., Hazarika, H. (2024). “Liquefaction damage in the Nishi Araya area of Uchinada Town due to the 2024 Noto Peninsula earthquake (part 2) - Damage investigation using UAV photogrammetry and 3D laser surveying.” *In: 59th Annual Conference of Japanese Geotechnical Society, Asahikawa, Japan*, paper ID: [23-12-2-08]. [in Japanese]

Murai, M., Hazarika, H., Matsumoto, T., Ohta, S., Kubota, S. (2024). “Liquefaction damage in the Muro district of Uchinada Town due to the 2024 Noto Peninsula earthquake- (Part 1): Topography, geology, and geological history.” *In: 59th Annual Conference of Japanese Geotechnical Society, Asahikawa, Japan*, paper ID: [25-13-1-01]. [in Japanese]

National Research Institute for Earth Science and Disaster Resilience (2024). “Source inversion analysis of the Noto Peninsula Earthquake (January 1, 2024, 16:10 JST, M7.6) using strong motion records.” https://www.kyoshin.bosai.go.jp/kyoshin/topics/noto_20240101/inversion/inv_index.html . [in Japanese]

National Research Institute for Earth Science and Disaster Resilience (2024). “Epicentral distribution and initial-motion focal mechanisms of major events during the 2024 Noto Peninsula Earthquake based on Hi-net data.” https://www.hinet.bosai.go.jp/topics/noto240101/?LANG=en&m=summary. [in Japanese]

Ota, Y., and Hirakawa, K. (1979). “Marine terraces and their deformation in Noto Peninsula, Japan Sea side of Central Japan.” *Geographical Review of Japan*, 52-4, 169-189, 1979

Ozaki, M., Inoue, T., Takagi, T., Komazawa M. and Okuma S. (2019). “Geological map of Japan 1:200,000, Wajima (2nd Edition).” *Geological Survey of Japan*, AIST, 2019

PDC Consortium, Japan: About PDC, https://www.pdc-cons.jp/en/about-pdc.html

Sahare, A., Qin, C., Hu, Y., Hazarika, H., Matsumoto, T., Tanaka, T. (2024). “Liquefaction damage in the Nishi Araya area of Uchinada Town due to the 2024 Noto Peninsula earthquake (Part 2) – Insights from the Nishi Araya elementary school.” *In: 59th Annual Conference of Japanese Geotechnical Society, Asahikawa, Japan*, paper ID: [23-12-2-07].

Senna, S. (2024). “Distribution and characteristics of liquefaction damage. In: Proceedings of the Symposium on the 2024 Noto Peninsula Earthquake, National Research Institute for Earth Science and Disaster Resilience.” https://www.bosai.go.jp/introduction/kyoso/kenkyukai/houkokukai_20240305.html.

Tanaka, T., Suemasa, N., Katada, T., and Yamato, S. (2014). “Evaluation of soil liquefaction potential by screw driving sounding test.” *In: Proc. of the Intl. Offshore and Polar Engineering Conference*, pp. 676-681.

Tani, K. (2016). “Development of the Konjyaku map: Distributing and browsing service on old topographic map tiles images.” *Theory and Applications of GIS, 25*(1), 1-10. [in Japanese].

United States Geological Survey (USGS). https://earthquake.usgs.gov/earthquakes/eventpage/us6000m0xl/executive. Retrieved 16 October 2024.